

1

2

3

4

## Search for flavor-changing neutral currents $tHq$ interactions with $H \rightarrow \tau^+\tau^-$ in proton-proton collisions at $\sqrt{s} = 13$ TeV

5

The ATLAS Collaboration

6

28th November 2020

7

8

9

10

11

12

13

14

15

16

A search is presented for flavor-changing neutral currents  $tHq$  interactions with  $H \rightarrow \tau^+\tau^-$  using a data set collected with the ATLAS detector at the LHC, corresponding to an integrated luminosity of  $140 \text{ fb}^{-1}$  of proton-proton collisions at a center-of-mass energy of 13 TeV. The search is performed in the decay chain  $t\bar{t} \rightarrow Wb + Hq$  or  $qg \rightarrow tH \rightarrow Wb + H$  ( $q = c/u$ ), where the  $W$  boson decays inclusively and  $H$  decays to  $\tau^+\tau^-$ . Upper limits at 95 % confidence level for the coupling coefficient are measured to be  $XXX$  and  $XXX$ , while the expected limits are  $XXX^{+XXX}_{-XXX}\%$  and  $XXX^{+XXX}_{-XXX}\%$ , respectively.

To be done:

1) Theory systematics

2) Systematics for lepton channels

17



# 1 Introduction

Since the discovery of the Higgs boson in 2012, great efforts are made to study its properties. As the mass of the Higgs boson is about 125 GeV [1], it is kinematically allowed that a top quark decays to a Higgs boson and an up-type quark via the flavour-changing neutral current (FCNC). In the Standard Model (SM), the FCNC interaction is forbidden at tree level and suppressed at higher orders due to the Glashow-Iliopoulos-Maiani (GIM) mechanism [2]. The  $t \rightarrow u/c + H$  branching fraction in the SM is calculated to be around  $10^{-15}$  [3]. It would be enhanced in many models beyond the SM (BSM). Examples are the quark-singlet model [4, 5], the two-Higgs doublet model with or without the flavour violation [6, 7], the minimal supersymmetric standard model (MSSM) [8], supersymmetry with R-parity violation [9], the Topcolour-assisted Technicolour model [10] or models with warped extra dimensions [11], the little Higgs model with T-parity conservation [12] and the composite Higgs models [13]. Especially, the ansatz of Cheng and Sher [14] allows a branching fraction of about  $10^{-3}$  [15]. Therefore, an observation of this decay would be a clear evidence for new physics.

On the other hand, if the  $tHq$  interaction exists, the single-top, Higgs associated production through this interaction should also be enhanced. The  $tH$  associated production in the SM prediction is expected to be small at LHC[16]. So the study on this process will also contribute to the FCNC interaction searches.

Upper 95% CL limits on  $\text{BR}(t \rightarrow Hq)$  have been obtained by ATLAS based on the data from 2015 and 2016, in the  $H \rightarrow \gamma\gamma$  [17],  $H \rightarrow WW/\tau_{\text{lep}}\tau_{\text{lep}}$  multilepton [18] and  $H \rightarrow \tau\tau$ ,  $H \rightarrow b\bar{b}$  [19] channels. The combined expected (observed) limits are 0.083% (0.11%) and 0.083% (0.12%) for  $t \rightarrow Hc$  and  $t \rightarrow Hu$ , respectively.

The  $t \rightarrow Hq$  decay and  $gq \rightarrow tH$  production are also searched by CMS based on the data from 2015 and 2016[20].

The FCNC coupling is parametrised using dim-6 operators [21]. The effective Lagrangian regarding  $tqH$  interaction before spontaneously symmetry breaking is:

$$\mathcal{L}_{EFT} = \frac{C_{u\phi}^{i3}}{\Lambda^2}(\phi^\dagger\phi)(\bar{q}_i t)\tilde{\phi} + \frac{C_{u\phi}^{3i}}{\Lambda^2}(\phi^\dagger\phi)(\bar{Q}u_i)\tilde{\phi} + H.c \quad (1)$$

Where the the operator notation is consistent with [21].  $C^{i3}$  is the Wilson coefficient of the 6-dim operator with  $i = 1, 2$  denoting the flavor of upper type quark.  $\Lambda$  is the scale of the new physics where the UV cut off happens which is set as 1 TeV as benchmark.  $\phi$  is the SM higgs doublet.  $\tilde{\phi} = \epsilon\phi^*$  where  $\epsilon$  is the antisymmetric matrix with  $\epsilon_{12} = -\epsilon_{21} = 1$ .

The Wilson coefficient  $C_{u\phi}$ 's can be extracted as

$$\begin{aligned} (C_{u\phi}^{i3})^2 + (C_{u\phi}^{3i})^2 &= 1946.6 \text{ BR}(t \rightarrow qH) \\ (C_{u\phi}^{13})^2 + (C_{u\phi}^{31})^2 &= \sigma(ug \rightarrow tH)/365.2 \text{ fb} \\ (C_{u\phi}^{23})^2 + (C_{u\phi}^{32})^2 &= \sigma(cg \rightarrow tH)/52.9 \text{ fb} \end{aligned} \quad (2)$$

To give a better impression on the numbers, we use  $\text{BR}(t \rightarrow qH) = 1(0.2)\%$  as benchmark, which is corresponding to  $(C_{u\phi}^{13})^2 + (C_{u\phi}^{31})^2 = 19.47(3.89)$ ,  $\sigma(ug \rightarrow tH) = 7109.0(1421.8)$  pb,  $\sigma(cg \rightarrow tH) = 1029.8(206.0)$  pb.

In this article, a search for the decay  $t \rightarrow qH$  in the  $t\bar{t}$  production (TT) and single-top, Higgs associated production (ST) with  $H \rightarrow \tau\tau$  as shown in Fig 1 using  $140 \text{ fb}^{-1}$  of proton-proton collision data at 13 TeV, taken with the ATLAS detector at the Large Hadron Collider (LHC), is presented. The final state is characterized by one top and one Higgs. In TT, there is an additional u/c quark forming a top resonance with Higgs.

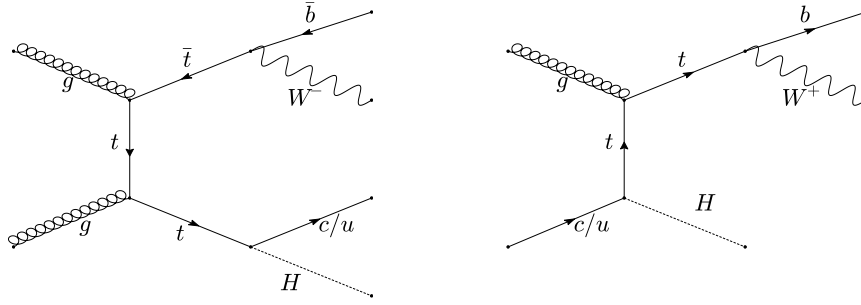


Figure 1: Diagrams of FCNC TT(left) and ST(right) process.

## 2 Detector, data set and Monte Carlo simulation

### 2.1 ATLAS detector

The ATLAS detector [22] at the LHC covers nearly the entire solid angle around the collision point. It consists of an inner tracking detector surrounded by a thin superconducting solenoid, electromagnetic and hadronic calorimeters, and a muon spectrometer incorporating three large superconducting toroid magnets.

The inner-detector system (ID) is immersed in a 2 T axial magnetic field and provides charged particle tracking in the range  $|\eta| < 2.5$ . A high-granularity silicon pixel detector covers the vertex region and typically provides three measurements per track. It is followed by a silicon microstrip tracker, which usually provides four two-dimensional measurement points per track. These silicon detectors are complemented by a transition radiation tracker, which enables radially extended track reconstruction up to  $|\eta| < 2.0$ . The transition radiation tracker also provides electron identification information based on the fraction of hits above a higher energy-deposit threshold corresponding to transition radiation. Compared to Run-1, an Insertable B-Layer [23] (IBL) is inserted as the innermost pixel layer during LS1 for Run-2, which significantly improves the tracking performance.

The calorimeter system covers the pseudorapidity range  $|\eta| < 4.9$ . Within the region  $|\eta| < 3.2$ , electromagnetic calorimetry is provided by barrel and endcap high-granularity liquid-argon (LAr) electromagnetic calorimeters, with an additional thin LAr presampler covering  $|\eta| < 1.8$ , to correct for energy loss in material upstream of the calorimeters. Hadronic calorimetry is provided by a scintillator-tile calorimeter, segmented into three barrel structures within  $|\eta| < 1.7$ , and two LAr hadronic endcap calorimeters.

A muon spectrometer (MS) comprises separate trigger and high-precision tracking chambers measuring the deflection of muons in a magnetic field generated by superconducting air-core toroids. The precision chamber system covers the region  $|\eta| < 2.7$  with three layers of monitored drift tubes, complemented by cathode strip chambers in the forward region, where the background is highest. The muon trigger system covers the range  $|\eta| < 2.4$  with resistive-plate chambers in the barrel, and thin-gap chambers in the endcap regions.

## 2.2 Data set

This analysis is based on the full proton-proton data at a center-of-mass energy  $\sqrt{s} = 13$  TeV with a bunch spacing of 25 ns collected by ATLAS in Run-2. The following good run list (GRL) was used for the 2015 dataset:

data15\_13TeV.periodAllYear\_DetStatus-v89-pro21-02

\_Unknown\_PHYS\_StandardGRL\_All\_Good\_25ns.xml

which corresponds to an integrated luminosity of  $3.22 \text{ fb}^{-1}$ .

The GRL used for the 2016 dataset:

data16\_13TeV.periodAllYear\_DetStatus-v89-pro21-01

\_DQDefects-00-02-04\_PHYS\_StandardGRL\_All\_Good\_25ns.xml

corresponds to an integrated luminosity of  $32.88 \text{ fb}^{-1}$ .

These GRLs exclude data where the IBL was not fully operational. The uncertainty in the combined 2015+2016 integrated luminosity,  $36.1 \text{ fb}^{-1}$ , is 2.1%. It is derived, following a methodology similar to that detailed in Ref. [24], from a calibration of the luminosity scale using x-y beam-separation scans performed in August 2015 and May 2016.

The GRL used for the 2017 dataset:

data17\_13TeV.periodAllYear\_DetStatus-v99-pro22-01

\_Unknown\_PHYS\_StandardGRL\_All\_Good\_25ns\_TriggerNo17e33prim.xml

corresponds to an integrated luminosity of  $44.307 \text{ fb}^{-1}$ .

The GRL used for the 2018 dataset:

```
data18_13TeV.periodAllYear_DetStatus-v102-pro22-04
_Unknown_PHYS_StandardGRL_All_Good_25ns_TriggerNo17e33prim.xml
```

corresponds to an integrated luminosity of  $59.937 \text{ fb}^{-1}$ . The final luminosity used for the analysis is  $140.45 \text{ fb}^{-1}$ .

## 2.3 Signal and background simulation

The overview of the major samples generated is summarized in table 1.

The TopFCNC UFO model [25, 26] with 5-flavour scheme is used for signal simulation.

The FCNC ST signal is simulated using MadGraph5\_aMC@NLO v2.6.2 [27] interfaced with Pythia 8 [28] with the A14 tune [29] for the generation of parton showers, hadronisation and multiple interactions and the NNPDF30NLO [30] parton distribution functions (PDF) is used to generate  $qg$  events at next-to-leading order (NLO) in QCD. Depending on either up quark or charm quark involved in the FCNC decay and either the  $W$  bosons decaying hadronically or leptonically, 4 samples are generated for each term of effective Lagrangian, so eight samples in total.

The FCNC TT signal is simulated using Powheg-Box [31] V2 interfaced with Pythia8 [28] with the A14 tune [29] for the generation of parton showers, hadronisation and multiple interactions and the NNPDF30NLO [30] parton distribution functions (PDF) is used to generate  $t\bar{t}$  events at next-to-leading order (NLO) in QCD. Depending on either the top or the anti-top quark decaying to  $bW$ , either up quark or charm quark involved in the FCNC decay and either the  $W$  bosons decaying hadronically or leptonically, eight samples are produced with the Higgs going to a  $\tau$ -lepton pair.

The dominant background is the  $t\bar{t}$  production. The  $t\bar{t}$  process and the single top process are generated with Powheg-Box [31] V2, and Pythia8 is used for the parton shower. NNPDF30NLO [30] and A14 tune [29] are used for  $t\bar{t}$ (single top). The  $t\bar{t}$  sample is also generated with different generators and parton showers models, as well as different amount of radiations, for systematics as detailed in Sec. 10.

The  $t\bar{t}X$ , where  $X=W, ee, \mu\mu, \tau\tau$  or  $Z(qq, \nu\nu)$  ( $\tau\tau$  has the Higgs resonance excluded), are generated with MadGraph5\_aMC@NLO and interfaced with Pythia8 for the parton shower. The NNPDF30NLO [30] is used for the matrix element PDF. The  $t\bar{t}$ , single top and  $t\bar{t}X$  are combined into a single process named top background in the analysis.

The  $W$ +jets,  $Z$ +jets and diboson backgrounds are simulated using Sherpa 2.2.1 [32] with NNPDF30NNLO PDF [30].

Table 1: Overview of the MC generators used for the main signal and background samples

Process	Generator		PDF set		Tune	Order
	ME	PS	ME	PS		
TT Signal	Powheg	Pythia8	NNPDF30NLO	NNPDF23LO	A14	NLO
ST Signal	MadGraph5_aMC@NLO	Pythia8	NNPDF30NLO	NNPDF23LO	A14	NLO
$W/Z$ +jets	Sherpa 2.2.1		NNPDF30NNLO		Sherpa	NLO/LO
$t\bar{t}$	Powheg	Pythia8	NNPDF30NLO	NNPDF23LO	A14	NLO
Single top	Powheg	Pythia6	CT10(NLO)	CTEQ6L1[44]	Perugia2012	NLO
$t\bar{t}X$	MadGraph5_aMC@NLO	Pythia8	NNPDF30NLO	NNPDF23LO	A14	NLO
Diboson	Sherpa 2.2.1		NNPDF30NNLO		Sherpa	NLO/LO

The  $\tau$  decay in the single top samples is handled by Tauola [33]. All samples showered by Pythia8 (Sherpa) have the  $\tau$  decays also handled by Pythia8 (Sherpa). All the decay modes of the  $\tau$  lepton are allowed in the event generators (but may be subject to generator filters). The summary of used generators for matrix element and parton shower is given in Tab. 1.

The SM higgs background includes  $ggH$ ,  $VH$ ,  $VBF$  and  $t\bar{t}H$ , generated from Powheg-Box [31] V2 interfaced with Pythia8. The overall contribution is pretty small. Various PDF and tune options are used for those samples depending on the decay modes.

The  $tH$  associated production is negligible but we still considered it. The sample is generated using MadGraph5 and interfaced with pythia8 for parton shower. CT10 PDF and A14 tune are used. It is treated as part of SM higgs background explained in above.

All Monte-Carlo (MC) samples were passed through the full GEANT4 [34] simulation of the ATLAS detector, except for two extra  $t\bar{t}$  samples with Pythia8 and Herwig7 [35] parton showering which are simulated with ATLAST-II [36] for systematics (Sec. 10). In the analysis, the simulated events were reweighted based on their pile-up to match the pile-up profile observed in data.

The full list of MC samples and their corresponding cross sections are given in App. ???. The single boson and diboson cross sections are calculated to NNLO [37]. The  $t\bar{t}$  cross section is calculated at NNLO in QCD including resummation of NNLL soft gluon terms for a top-quark mass of 172.5 GeV [38]. The  $t\bar{t}H$  and  $t\bar{t}V$  are normalized to NLO cross sections according to [39] and [40]. The  $t$ -channel and  $s$ -channel single top cross sections are calculated at NLO with Hathor v2.1 [41, 42], while the  $Wt$  channel is calculated at NLO+NNLL [43].

### 3 Object reconstruction

In this section, various objects used in this analysis are defined, namely jets, electrons, muons, hadronically decaying taus and missing transverse energy.

### 3.1 Jets

Jets are reconstructed using the anti- $k_t$  algorithm [45] with a distance parameter  $R = 0.4$  applied to the particle flow candidates. Only jets with  $p_T > 25$  GeV and  $|\eta| < 4.5$  are considered by the analysis. To suppress jets produced in additional pile-up interactions, jets with  $p_T < 60$  GeV and  $|\eta| < 2.4$  are required to have a Jet Vertex Tagger (JVT [46]) parameter larger than 0.2 (Medium working point). The JVT is the output of the jet vertex tagger algorithm used to identify and select jets originating from the hard-scatter interaction through the use of tracking and vertexing information. About 10% of selected jets in the signal are in the forward detector region. After the above selection and overlap removal, a “jet cleaning” cut performed by JetCleaningTool with LooseBad working point is applied on all the jets, and the events with jets not passing this cut are discarded.

### 3.2 b-tagging

The DL1r [47] algorithm is used to identify the jets initiated by  $b$ -quarks. A working point corresponding to an average efficiency of 70% for jets containing  $b$ -quarks is chosen.

### 3.3 Electrons

Electron candidates are identified by tracks reconstructed in the inner detector and the matched cluster of energy deposited in the electromagnetic calorimeter. Electrons candidates are required to have  $E_T > 15$  GeV and  $|\eta| < 2.47$ . The transition region,  $1.37 < |\eta| < 1.52$ , between the barrel and end-cap calorimeters is excluded. They are further required to pass a loose + b-layer likelihood-based identification point [48] and a FCLoose isolation working point [49]. The electrons are further removed if its cluster is affected by the presence of a dead frontend board in the first or second sampling or by the presence of a dead high voltage region affecting the three samplings or by the presence of a masked cell in the core.

### 3.4 Muons

Muon reconstruction begins with tracks reconstructed in the MS and is matched to tracks reconstructed in the inner detector. Muon candidates are required to have  $p_T > 10$  GeV and  $|\eta| < 2.5$ . A Loose identification selection [50] based on the requirements on the number of hits in the ID and the MS is satisfied. A Gradient isolation [49] criterion is also required.



### 3.5 Hadronic tau decays

The hadronic tau candidates [51] are seeded by jets reconstructed by the anti- $k_t$  algorithm [45], which is applied on calibrated topo clusters [52] with a distance parameter of  $R=0.4$ . They are required to have  $p_T > 20$  GeV and  $|\eta| < 2.5$ . The transition region between the barrel and end-cap calorimeters ( $1.37 < |\eta| < 1.52$ ) is excluded. An identification algorithm based on Recursive Neural Network [53] is applied to discriminate the visible decay products of hadronically decaying tau lepton  $\tau_{\text{had}}$  from jets initiated by quarks or gluons. Different RNN working points are provided and required at different levels depending on the analysis channel. The Loose ID taus are used for the overlap removal and missing transverse energy calculation. In the analysis event selection, the hadronic tau candidates are required to have one or three charged tracks and an absolute charge of one, and pass the Medium tau ID to reject the jets. For the Medium ID, the tau efficiency is about 75% (60%) for 1-prong (3-prong) candidates. The ID efficiencies are optimized to be flat versus the tau  $p_T$  and pileup. The tau candidates are required to not overlap with a very loose electron candidate, and a dedicated BDT variable is also used to veto the taus which are actually electrons. If the  $\tau_{\text{had}}$  candidate is also tagged as a  $b$ -jet, then this tau object is also not used. Efficiency scale factors for tau reconstruction, ID and electron BDT rejection [54] are applied on tau candidates in MC.

### 3.6 Missing transverse energy

The missing transverse energy  $E_T^{\text{miss}}$  is computed using the fully calibrated and reconstructed physics objects as described above. The TrackSoftTerm (TST) algorithm is used to compute the SoftTerm of the  $E_T^{\text{miss}}$  [55].

### 3.7 Overlap removal

For the objects passing the selection above, a geometric overlap removal is applied to eliminate the ambiguity in the object identification. When two objects are close geometrically with  $\Delta R$  less than a certain threshold, or satisfy some certain requirements, one of them will be removed. The overlap removal is done by the official overlap removal tool provided by ASG group. The "Standard" working point is used. The rules are described as follows in sequence:

- If two electrons have overlapped second-layer cluster, or shared tracks, the electron with lower  $p_T$  is removed.
- $\tau_{\text{had}}$  within a  $\Delta R = 0.2$  cone of an electron or muon are removed.

- If a muon sharing an ID track with an electron and the muon is calo-tagged, the muon is removed. Otherwise the electron is removed.
- Jets within a  $\Delta R = 0.2$  cone of an electron are removed.
- Electrons within a  $\Delta R = 0.4$  cone of a jet are removed.
- When a muon ID track is ghost associated to a jet or within a  $\Delta R = 0.2$  cone of a jet, the jet is removed if it has less than 3 tracks with  $p_T > 500$  MeV or has a relative small  $p_T$  ( $p_T^\mu > 0.5 p_T^{\text{jet}}$  and  $p_T^\mu > 0.7$ [the scalar sum of the  $p_T$ 's of the jet tracks with  $p_T > 500$  MeV]).
- Muons within a  $\Delta R = 0.4$  cone of a jet are removed.
- Jets within a  $\Delta R = 0.2$  cone of the leading  $\tau_{\text{had}}$  ( $\tau_{\text{lep}}\tau_{\text{had}}$ ), or with the two leading  $\tau_{\text{had}}$ 's ( $\tau_{\text{had}}\tau_{\text{had}}$ ), are excluded. The overlap also works for the reverted tau ID regions used in the analysis, since the tau ID information is not used.
- If a tau object is also tagged as a  $b$ -jet, then this event is removed.

Note that the  $E_T^{\text{miss}}$  calculation package has its own overlap removal procedure. Taus that fail Loose ID are also passed to the package. Only two leading taus are considered in the calculation.

Table 2: Overview of the final states of signal events

	# of particles	alias	b-jet	jets	lepton	taus
ST	$W \rightarrow l\nu$	STL	1	1	1	2
	$W \rightarrow q\bar{q}$	STH	1	3	0	2
TT	$W \rightarrow l\nu$	TTL	1	2	1	2
	$W \rightarrow q\bar{q}$	TTH	1	4	0	2

Table 3: Overview of the signal regions

# of particles	b-jet	light flavor jets	lepton	hadronic taus
$l\tau_{\text{had}}(\text{SS}) 2j$	1	2	1	1
$l\tau_{\text{had}}(\text{SS}) 1j$	1	1	1	1
$l\tau_{\text{had}}\tau_{\text{had}}(\text{OS})$	1	$\geq 0$	1	2
STH $\tau_{\text{had}}\tau_{\text{had}}(\text{OS})$	1	2	0	2
TTH $\tau_{\text{had}}\tau_{\text{had}}(\text{OS})$	1	$\geq 3$	0	2
STH $\tau_{\text{lep}}\tau_{\text{had}}(\text{OS})$	1	2	1	1
TTH $\tau_{\text{lep}}\tau_{\text{had}}(\text{OS})$	1	$\geq 3$	1	1

## 4 Blinding strategy

In order to keep the analysis unbiased from artificial cut tunings, data histogram bins with significances greater than 1 when decaying branching ratio is 0.2% are blinded. In addition, the signal enriched high BDT region are blinded (BDT > 0.2).

## 5 Reconstruction of event topology

Depending on the production modes and the decay of the  $W$  boson from top quark, the analysis is split into 4 categories as shown in table 2. Except events with 2 leptons (leptonic tau included) or no hadronic tau in the final states, all of the decay modes are considered in the analysis. The selection requirement dedicated for most sensitive decay modes are listed in table 3 where the sensitive cut off is 1 sigma for  $B(t \rightarrow Hq)$  of 0.2%. Due to the low statistics when STL cuts are applied, the STL and TTL are included in a single region  $l\tau_{\text{had}}\tau_{\text{had}}$  for  $H \rightarrow \tau_{\text{had}}\tau_{\text{had}}$  where there is no light jet multiplicity requirement. However due to the low tau reconstruction rate, it is not rare that one of tau fails the reconstruction and remains as a jet. So the  $l\tau_{\text{had}} 1j$  and  $l\tau_{\text{had}} 2j$  are included as signal regions where the lepton and  $\tau_{\text{had}}$  are same charged to reduce background.

For the future convenience, STH  $\tau_{\text{lep}}\tau_{\text{had}}$  and TTH  $\tau_{\text{lep}}\tau_{\text{had}}$  are indicated by  $\tau_{\text{lep}}\tau_{\text{had}}$ ; STH  $\tau_{\text{had}}\tau_{\text{had}}$  and TTH  $\tau_{\text{had}}\tau_{\text{had}}$  are indicated by  $\tau_{\text{had}}\tau_{\text{had}}$ ;  $l\tau_{\text{had}} 2j$  and  $l\tau_{\text{had}} 1j$  are indicated by  $l\tau_{\text{had}}$ . All the channels involving leptons (including  $\tau_{\text{lep}}$ ) are indicated by leptonic channels.

To comply with the signal topology, in each channel, exactly one jet should be tagged as a  $b$ -jet.

In TTH channel, all jets from the top hadronic decay and the jet from  $t \rightarrow Hq$ , denoted as the FCNC jet, pass the jet selection, there should be at least four jets among which the one with smallest  $\Delta R(p_{\text{jet}}^\mu, p_{\tau 1}^\mu + p_{\tau 2}^\mu)$  is considered as FCNC jet. If there are more than 2 jets beside FCNC jet and  $b$ -jet, the jets from  $W$  boson decay are chosen from the combination which have the invariant mass closest to  $W$  resonance. There is the chance that one of the jets fails the  $p_T$  requirement and not reconstructed. This kind of events will fall into STH channel. The FCNC top resonance is still reconstructed given the big chance that the jet which is missing is from  $W$  decay.

In STH events, there are 3 jets coming from top decay including the  $b$ -jet. So a Higgs resonance formed by the taus and a top resonance formed by the jets are expected.

In STH and TTH channels, the  $\chi^2$  fit is used to reconstruct the ditau mass and momentum by taking the  $\tau$  decay kinematics into account. To determine the 4-momenta of the invisible decay products of the tau decays, the following  $\chi^2$  in Eq. 3, based on the collinear approximation is used.

$$\chi^2 = \left( \frac{m_H^{\text{fit}} - 125}{\sigma_{\text{Higgs}}} \right)^2 + \left( \frac{E_{x,\text{miss}}^{\text{fit}} - E_{x,\text{miss}}}{\sigma_{\text{miss}}} \right)^2 + \left( \frac{E_{y,\text{miss}}^{\text{fit}} - E_{y,\text{miss}}}{\sigma_{\text{miss}}} \right)^2, \quad (3)$$

In Eq. 3, the free parameters scanned are the energy ratio of invisible decay products for each tau decay. If the tau decays leptonically, the neutrino mass is also introduced in the fit which is constrained to be smaller than tau mass. The Higgs mass resolution is set to 1.8 GeV and 20 GeV respectively. The  $E_T^{\text{miss}}$  resolution is parametrized as

$$\sigma_{\text{miss}} = 13.1 + 0.50\sqrt{\Sigma E_T}, \quad (4)$$

where  $\Sigma E_T$  (in GeV) is the scalar sum of transverse energy depositions of all objects and clusters. The invisible 4-momenta are obtained by minimizing the combined  $\chi^2$  for each event. By adding the Higgs mass constraint term in the kinematic fit, not only is the Higgs mass resolution improved, but also the resolutions of the Higgs boson's four-momentum, and the mass of the top from which the Higgs comes. Figure 2 shows the distributions of  $\chi^2$  in different regions. Good agreement between data and background predictions are achieved.

In  $l\tau_{\text{had}}\tau_{\text{had}}$  channels, a Higgs resonance formed by the taus is expected. Additionally for TTL  $\tau_{\text{had}}\tau_{\text{had}}$  events, a top resonance formed by the  $c/u$  jet and Higgs is expected.

Due to the large amount of neutrinos produced in leptonic channels with a huge degree of freedom. The kinematic fit to reconstruct the neutrinos is given up in  $l\tau_{\text{had}}\tau_{\text{had}}$  and  $l\tau_{\text{had}}$  channels. The kinematics calculated directly from visible particles and  $E_T^{\text{miss}}$  are used as BDT input.

With the event topology reconstructed, a number of variables are defined for signal and background separation. Their distributions can be found in Sec. 8, and some of their explanations are as follows. In the following explanations, di-tau point to the visible decay product of both  $\tau_{\text{had}}$  and  $\tau_{\text{lep}}$ .

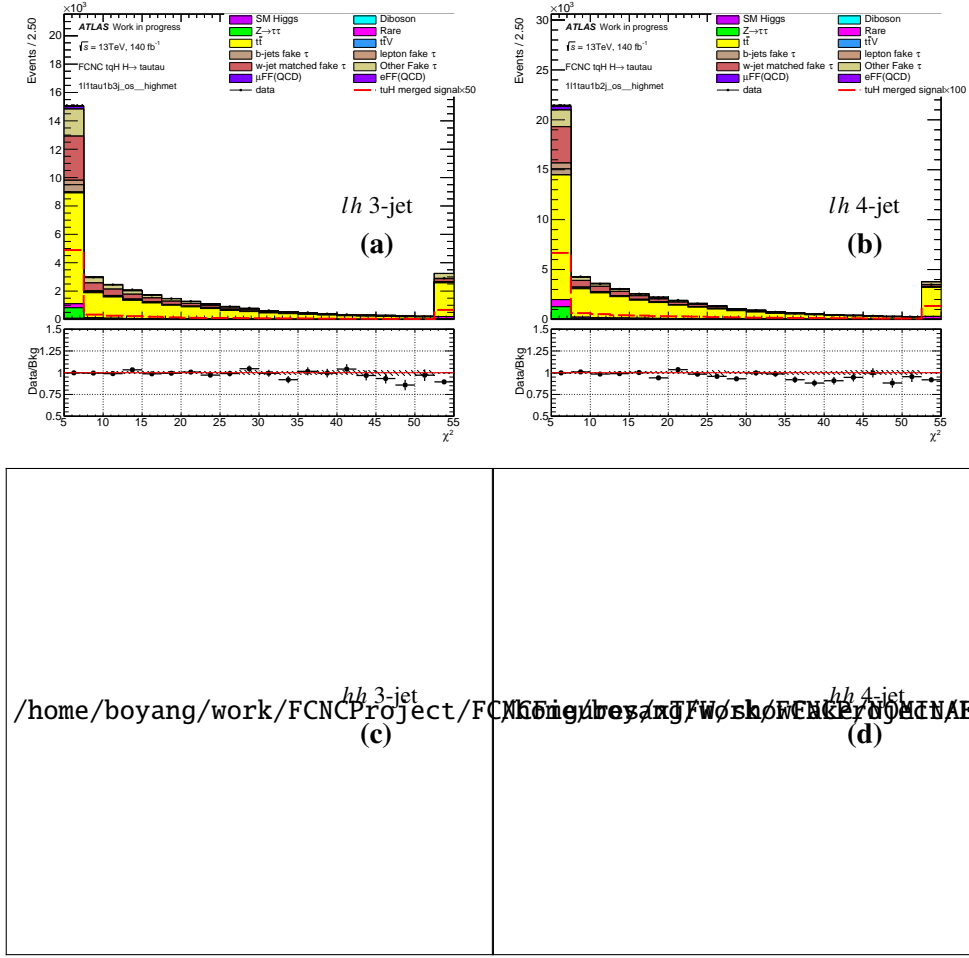


Figure 2: The distributions of  $\chi^2$  in Eq. 3 in the hadronic channels.

1.  $E_{miss}^T$  is the missing transverse momentum.
2.  $p_{T,\tau}$  is the transverse momentum of the leading tau candidate.
3.  $p_{T,sub-\tau}$  is the transverse momentum of the sub-leading tau candidate.
4.  $p_{T,l}$  is the transverse momentum of the leading lepton.
5.  $\chi^2$  is derived from kinematic fitting for the neutrinos.
6.  $m_{t,SM}$  is the invariant mass of the  $b$ -jet and the two jets from the  $W$  decay, and reflects the top mass in the decay  $t \rightarrow Wb \rightarrow j_1 j_2 b$ . This variable is only defined for the 4-jet STH and TTH events.
7.  $m_W^T$  is the transverse mass calculated from the lepton and  $E_{miss}^T$  in the leptonic channels, defined as

$$m_W^T = \sqrt{2p_{T,lep}E_{miss}^T(1 - \cos \Delta\phi_{lep,miss})}. \quad (5)$$

8.  $m_{\tau,\tau}$  is the invariant mass of the tau candidates and reconstructed neutrinos in STH and TTH channels.
9.  $m_W$  is the reconstructed invariant mass of the hadronic  $W$  boson from SM top quark.
10.  $m_{t,FCNC}$  is the visible invariant mass of the FCNC-decaying top quark reconstructed from di-tau candidates, FCNC-jet and reconstructed neutrinos.
11.  $m_{\tau\tau,vis}$  is the visible invariant mass of the di-tau candidates
12.  $p_{T,\tau\tau,vis}$  is the  $p_T$  of the di-tau candidates.
13.  $m_{t,FCNC,vis}$  is the reconstructed invariant mass of the FCNC-decaying top quark.
14.  $m_{t,SM,vis}$  is the invariant mass of the lepton and the b-jet, which reflects the visible SM top mass.
15.  $M(\tau\tau_{light} - jet, min)$  is the invariant mass of the di-tau candidates (include leptonic tau) and the light-flavor jet, minimized by choosing different jet.
16.  $M(light - jet, light - jet, min)$  is the invariant mass of two light-flavor jet, minimized by choosing different jets.
17.  $E_{miss}^T$  centrality is a measure of how central the  $E_T^{miss}$  lies between the two tau candidates in the transverse plane, and is defined as

$$E_T^{miss} \text{ centrality} = (x + y) / \sqrt{x^2 + y^2}, \quad (6)$$

$$\text{with } x = \frac{\sin(\phi_{miss} - \phi_{\tau_1})}{\sin(\phi_{\tau_2} - \phi_{\tau_1})}, y = \frac{\sin(\phi_{\tau_2} - \phi_{miss})}{\sin(\phi_{\tau_2} - \phi_{\tau_1})},$$

18.  $E_{v,i}/E_{\tau,i}, i = 1, 2$  is the momentum fraction carried by the visible decay products from the tau mother. It is based on the best-fit 4-momentum of the neutrino(s) according to the event reconstruction algorithm in this section. For the  $\tau_{had}$  decay mode, the visible decay products carry most of the tau energy since there is only a single neutrino in the final state, which is evident in the excess around 1 in Fig. 3.
19.  $\Delta R(l + b - jet, \tau + \tau)$  is the angular distance between the lepton+b-jet and di-tau candidates.
20.  $\Delta R(l, b - jet)$  is the angular distance between the lepton and b-jet.
21.  $\Delta R(\tau, b - jet)$  is the angular distance between the tau and b-jet.
22.  $\eta_{\tau,max}$  is the larger polar angle among the tau candidates.
23.  $\Delta R(l, \tau)$  is the angular distance between the lepton and the closest tau candidate in the leptonic channels.
24.  $\Delta R(\tau, fcnc - j)$  is the angular distance between the tau and the reconstructed fcnc jet.

- 306 25.  $\Delta R(\tau, \tau)$  is the angular distance between two tau candidates.
- 307 26.  $\Delta R(\tau, light - jet, min)$  is the angular distance between the closest tau candidate and light-flavor  
308 jet.
- 309 27.  $\Delta\phi(\tau\tau, P_{miss}^T)$  is the azimuthal angle between the  $E_T^{miss}$  and di-tau  $p_T$ .

## 6 Selection of events

In the leptonic channels, the  $p_T$  of the lepton is required to be 1 GeV above the trigger threshold. The leptons are required to have Tight ID as defined in Sec. 3.

In the hadronic channels, no leptons (as defined in Sec. 3) should be present in the event, and the two tau candidates with the highest  $p_T$  are chosen. They should also pass the Medium tau ID and overlap removal. To account for the trigger thresholds, the two hadronic taus are required to pass the  $p_T > 40$  GeV and  $p_T > 30$  GeV cuts.

### 6.1 Trigger

In the leptonic channels, the single-lepton triggers and di-lepton triggers are required to select the candidate events. In general, the lowest unprescaled triggers are used in every data-taking periods:

Single electron:

2016,2017,2018:

- HLT\_e26\_lhtight\_nod0\_ivarloose
- HLT\_e60\_lhmedium\_nod0
- HLT\_e140\_lhloose\_nod0

2015:

- HLT\_e24\_lhmedium\_L1EM20VH
- HLT\_e60\_lhmedium
- HLT\_e120\_lhloose

Single muon:

2016,2017,2018:

- HLT\_mu26\_ivarmedium
- HLT\_mu50

2015:

- HLT\_mu20\_iloose\_L1MU15
- HLT\_mu50



Di-electron:

2017,2018:

- HLT\_2e24\_lhvloose\_nod0

2016:

- HLT\_2e17\_lhvloose\_nod0

2015:

- HLT\_2e12\_lhloose\_L12EM10VH

Di-muon:

2016,2017,2018:

- HLT\_mu22\_mu8noL1

2015:

- HLT\_mu18\_mu8noL1

Election+Muon:

2016,2017,2018:

- HLT\_e17\_lhloose\_nod0\_mu14

2015:

- HLT\_e17\_lhloose\_mu14

The trigger matching between the offline and trigger level lepton objects is also required for the corresponding leptons selected for the analysis. The minimum offline lepton  $p_T$  should be 1 GeV above the trigger threshold. For the  $\tau_\mu\tau_{\text{had}}$  channel in 2016, the offline muon  $p_T$  is 2 GeV above the trigger threshold due to the trigger scale factors' binning<sup>1</sup>.

The trigger used for hadronic channels in each year are listed as follow:

- 2015: HLT\_tau35\_medium1\_tracktwo\_tau25\_medium1\_tracktwo\_L1TAU20IM\_2TAU12IM
- 2016: HLT\_tau35\_medium1\_tracktwo\_tau25\_medium1\_tracktwo
- 2017: HLT\_tau35\_medium1\_tracktwo\_tau25\_medium1\_tracktwo\_03dR30\_L1DR\_TAU20ITAU12I\_J25

<sup>1</sup> The trigger  $p_T$  cuts on the leptons are independent of and additional to the other  $p_T$  cuts introduced previously. For example, the  $p_T$  cuts used in the overlap removal are still as those in Sec. 3. It is also the case for the cuts introduced in the AOD derivations (Sec. 6.2).

• 2018: HLT\_tau35\_medium1\_tracktwoEF\_tau25\_medium1\_tracktwoEF\_03dR30\_L1DR\_TAU20ITAU12I\_J2

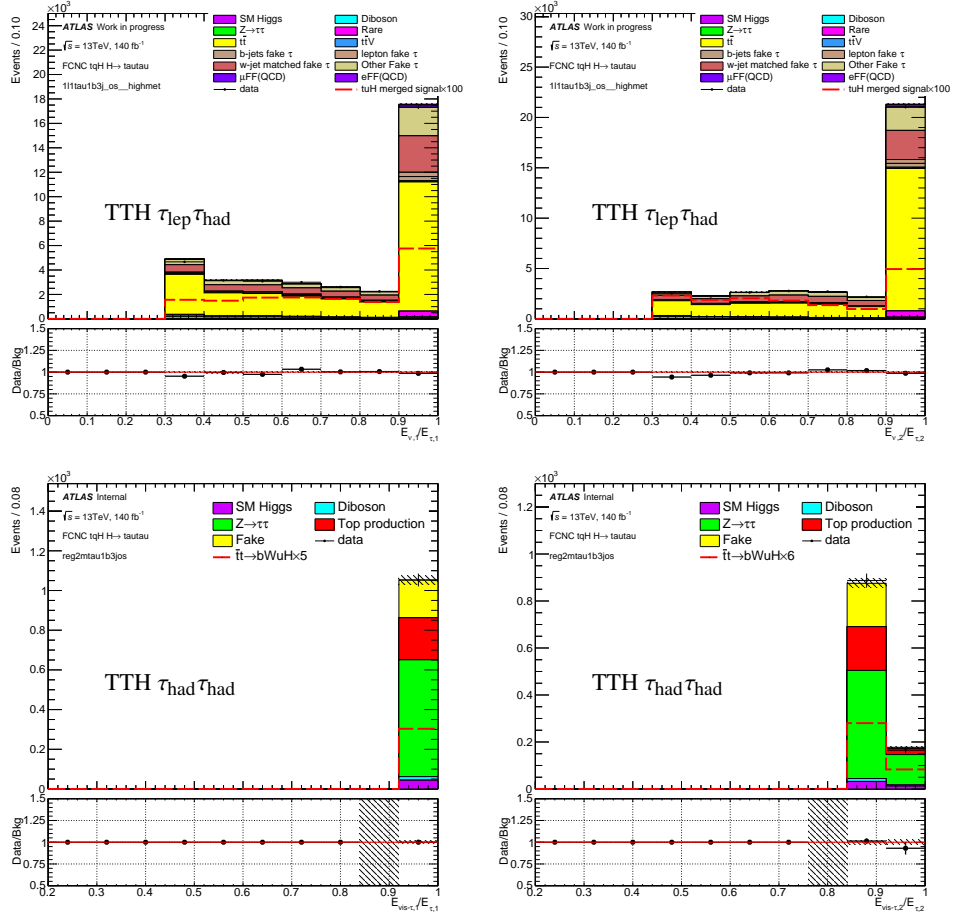
The two  $\tau_{\text{had}}$  candidates are matched to the respective legs of the di-tau trigger using the individual single tau trigger objects. The  $p_T$  thresholds are chosen such that the selected  $\tau_{\text{had}}$  candidate  $p_T$  already lies in the plateau of the respective trigger efficiency curve. Due to the rising instantaneous luminosity, the trigger used in the 2016 data taking includes a requirement for an additional level-1 calorimeter trigger jet with  $p_T > 25$  GeV and  $|\eta| < 3.2$ . The leading jet in the 2016 events is required to be matched within  $\Delta R < 0.4$  with the jet ROI that fulfilled the jet part of the trigger criteria (trigger jet). Figure ?? shows the turn-on curves of the additional jet as in [57], and the leading jet  $p_T$  in the  $\tau_{\text{had}}\tau_{\text{had}}$  channel. A cut of  $p_T^{\text{Ljet}} > 50$  GeV is required on the trigger jet, and a leading-jet  $p_T > 60$  GeV cut is applied to remove the effect of turn on curve.

## 6.2 Event cuts and regions

A number of event cuts are applied before getting to the signal enhanced regions with the background suppressed. Then the DAOD\_HIGG8D1 (DAOD\_HIGG4D3) derivation is feed to ttHMultiAna (xTauFramework) to produce n-tuples for analysis. The list of event-level selection criteria is as follows:

1. DAOD\_HIGG8D1 (leptonic channels) and DAOD\_HIGG4D3 ( $\tau_{\text{had}}\tau_{\text{had}}$ ) derivations are used for this analysis. At the derivation level, the following cuts are applied:
  - In DAOD\_HIGG8D1, trigger skimming: all election, muon, tau triggers; Offline skimming: at least 2 light leptons or at least 1 lepton plus 1 tau.
  - In DAOD\_HIGG4D3, no trigger skimming. Offline skimming: 2taus
2. At the xTauFramework level, skim cuts are applied to reduce the ntuple size:
  - No leptons, at least 1 medium tau and 1 loose tau, at least 3 jets with  $p_T > 30$  GeV,  $|\eta| < 4.5$  and passing either central or forward JVT cuts and with at least 1 b-tagged, pass di-tau trigger, LooseBad Event Cleaning, leading tau  $p_T > 40$  GeV, sub-leading tau  $p_T > 30$  GeV, two taus comes from a single vertex, leading jet  $p_T > 60$  GeV, leading jet  $|\eta| < 3.2$ ,  $E_T^{\text{miss}} > 15$  GeV. In the case of data, GRL cut as defined in Sec. 2.2 is also applied.
3. At the ttHMultiAna level, skim cuts [58] are applied to reduce the ntuple size.
4. At least one primary vertex exists in the event. The primary vertex is defined as the vertex that has the largest sum of track  $p_T^2$  associated to it, and has at least 4 tracks with  $|z_0| < 100$  mm.
5. The tau candidtes expected from Higgs decay should pass the Medium ID and the other quality cuts in Sec. 3.
6. It is required that the tau objects are not  $b$ -tagged, otherwise the event is rejected.

392

7. Exactly one  $b$ -tagged jets.Figure 3: The distributions of  $x_{1,2}^{fit}$  in the TTH  $\tau_{lep}\tau_{had}$  (top) and  $\tau_{had}\tau_{had}$  (bottom) channels.

393

The cutflow for the preselection and each channel are given in Table ?? - ??.

394

For the TT channel  $t\bar{c}H$  coupling search, the FCNC jet is from a  $c$ -quark. Regarding the similarity between the  $b$ -jet and  $c$ -jet, the very loose  $b$ -tagging is attempted on the FCNC jet in order to further select the  $t\bar{c}H$  signal. However, the dominating background is  $t\bar{t}$  where there are 2  $b$ -jets. This resort does not help with the significance.

397

Table 4: The cutflow tables for the preselection in the leptonic channels.

	SM Higgs	W+jets	Diboson	$Z \rightarrow ll$
n-tuple	17152.85 $\pm$ 102.09	2549803.66 $\pm$ 9945.07	259417.38 $\pm$ 334.63	5076218.50 $\pm$ 8306.74
pass trigger	16477.69 $\pm$ 100.32	2518835.54 $\pm$ 9889.11	248536.30 $\pm$ 333.15	4704322.06 $\pm$ 7984.34
leadtauOLR	16087.82 $\pm$ 99.05	2419309.44 $\pm$ 9772.39	240069.04 $\pm$ 325.01	4414736.28 $\pm$ 7728.34
subtauOLR	16082.01 $\pm$ 99.04	2418923.49 $\pm$ 9772.00	239973.79 $\pm$ 324.92	4413931.08 $\pm$ 7727.78
trigger match	15981.81 $\pm$ 98.70	2406789.97 $\pm$ 9746.08	239082.36 $\pm$ 324.18	4405527.85 $\pm$ 7722.63
tight lepton	14974.32 $\pm$ 95.86	2325820.71 $\pm$ 9589.35	225676.03 $\pm$ 318.63	3596467.15 $\pm$ 6321.88
Medium,25GeV leadtau	11671.30 $\pm$ 82.68	705359.50 $\pm$ 4980.18	149254.77 $\pm$ 199.43	2765958.95 $\pm$ 4754.76
Medium,25GeV subtau	11613.22 $\pm$ 82.49	702120.36 $\pm$ 4970.87	148609.89 $\pm$ 198.85	2763634.87 $\pm$ 4751.81
SR+CR	392.77 $\pm$ 9.55	9148.62 $\pm$ 258.83	1442.22 $\pm$ 22.99	3501.90 $\pm$ 106.01

	$Z \rightarrow \tau\tau$	Rare	$t\bar{t}$	$t\bar{t}V$
n-tuple	569469.50 $\pm$ 2600.27	279736.04 $\pm$ 187.62	3580387.63 $\pm$ 698.29	18645.78 $\pm$ 15.01
pass trigger	559082.94 $\pm$ 2582.60	267927.73 $\pm$ 183.83	3404908.11 $\pm$ 681.77	17674.85 $\pm$ 14.65
leadtauOLR	546917.05 $\pm$ 2556.75	261995.50 $\pm$ 181.81	3331840.00 $\pm$ 674.43	17395.55 $\pm$ 14.52
subtauOLR	546819.15 $\pm$ 2556.61	261936.09 $\pm$ 181.79	3330895.23 $\pm$ 674.33	17387.40 $\pm$ 14.51
trigger match	539963.88 $\pm$ 2537.77	260875.18 $\pm$ 181.43	3312474.25 $\pm$ 672.52	17278.52 $\pm$ 14.47
tight lepton	515237.69 $\pm$ 2485.89	240749.74 $\pm$ 174.41	3036019.50 $\pm$ 644.25	15835.21 $\pm$ 13.85
Medium,25GeV leadtau	332992.81 $\pm$ 1959.33	207144.85 $\pm$ 161.77	2646376.07 $\pm$ 601.22	14330.23 $\pm$ 13.00
Medium,25GeV subtau	331682.04 $\pm$ 1956.04	206920.51 $\pm$ 161.68	2643224.28 $\pm$ 600.86	14286.45 $\pm$ 12.98
SR+CR	3598.56 $\pm$ 52.46	8348.47 $\pm$ 32.26	161797.56 $\pm$ 148.42	1122.99 $\pm$ 4.12

	$t\bar{t} \rightarrow bWcH$	$cg \rightarrow tH$	tcH merged signal	$t\bar{t} \rightarrow bWuH$
n-tuple	2697.69 $\pm$ 4.51	124.01 $\pm$ 0.33	2821.70 $\pm$ 4.53	2697.40 $\pm$ 4.47
pass trigger	2591.28 $\pm$ 4.43	119.06 $\pm$ 0.33	2710.34 $\pm$ 4.44	2592.75 $\pm$ 4.38
leadtauOLR	2561.17 $\pm$ 4.40	117.83 $\pm$ 0.32	2678.99 $\pm$ 4.42	2565.50 $\pm$ 4.36
subtauOLR	2554.93 $\pm$ 4.40	117.50 $\pm$ 0.32	2672.43 $\pm$ 4.41	2560.52 $\pm$ 4.36
trigger match	2499.80 $\pm$ 4.35	114.99 $\pm$ 0.32	2614.78 $\pm$ 4.36	2507.98 $\pm$ 4.31
tight lepton	2299.96 $\pm$ 4.17	105.90 $\pm$ 0.31	2405.86 $\pm$ 4.18	2308.31 $\pm$ 4.13
Medium,25GeV leadtau	1889.15 $\pm$ 3.75	88.14 $\pm$ 0.28	1977.29 $\pm$ 3.76	1895.11 $\pm$ 3.72
Medium,25GeV subtau	1826.74 $\pm$ 3.69	84.68 $\pm$ 0.27	1911.43 $\pm$ 3.70	1829.31 $\pm$ 3.66
SR+CR	553.80 $\pm$ 2.08	25.73 $\pm$ 0.15	579.53 $\pm$ 2.09	552.12 $\pm$ 2.05

	$ug \rightarrow tH$	tuH merged signal	Data
n-tuple	631.43 $\pm$ 1.70	3328.82 $\pm$ 4.78	14388438.00 $\pm$ 3793.21
pass trigger	608.67 $\pm$ 1.67	3201.42 $\pm$ 4.69	13747432.00 $\pm$ 3707.75
leadtauOLR	601.45 $\pm$ 1.66	3166.96 $\pm$ 4.67	13183266.00 $\pm$ 3630.88
subtauOLR	599.85 $\pm$ 1.66	3160.37 $\pm$ 4.66	13181031.00 $\pm$ 3630.57
trigger match	589.11 $\pm$ 1.65	3097.09 $\pm$ 4.62	13113541.00 $\pm$ 3621.26
tight lepton	541.21 $\pm$ 1.58	2849.51 $\pm$ 4.42	11318527.00 $\pm$ 3364.30
Medium,25GeV leadtau	442.90 $\pm$ 1.42	2338.01 $\pm$ 3.98	7534936.00 $\pm$ 2744.98
Medium,25GeV subtau	427.94 $\pm$ 1.40	2257.24 $\pm$ 3.92	7524509.00 $\pm$ 2743.08
SR+CR	129.71 $\pm$ 0.78	681.83 $\pm$ 2.19	186660.00 $\pm$ 432.04

Table 5: The cutflow tables in the  $l\tau_{\text{had}}$  1j signal region.

	SM Higgs	W+jets	Diboson	$Z \rightarrow ll$
this region	$9.06 \pm 1.77$	$1880.37 \pm 103.44$	$122.06 \pm 9.92$	$487.10 \pm 39.28$
tau b-veto	$7.18 \pm 1.42$	$1813.01 \pm 98.27$	$118.61 \pm 9.91$	$469.90 \pm 39.05$
	$Z \rightarrow \tau\tau$	Rare	$t\bar{t}$	$t\bar{t}V$
this region	$58.59 \pm 16.01$	$467.01 \pm 7.56$	$4164.41 \pm 24.09$	$32.78 \pm 0.50$
tau b-veto	$56.33 \pm 15.77$	$422.87 \pm 7.21$	$3468.88 \pm 22.05$	$31.25 \pm 0.48$
	$\bar{t}t \rightarrow bWcH$	$cg \rightarrow tH$	tcH merged signal	$\bar{t}t \rightarrow bWuH$
this region	$61.43 \pm 0.61$	$2.38 \pm 0.04$	$63.81 \pm 0.61$	$62.49 \pm 0.62$
tau b-veto	$59.37 \pm 0.60$	$2.31 \pm 0.04$	$61.69 \pm 0.60$	$60.87 \pm 0.61$
	$ug \rightarrow tH$	tuH merged signal	Data	
this region	$12.03 \pm 0.21$	$74.52 \pm 0.65$	$8402.00 \pm 91.66$	
tau b-veto	$11.64 \pm 0.21$	$72.51 \pm 0.65$	$7563.00 \pm 86.97$	

Table 6: The cutflow tables in the STH  $\tau_{\text{lep}}\tau_{\text{had}}$  signal region.

	SM Higgs	W+jets	Diboson	$Z \rightarrow ll$
this region	$44.95 \pm 4.35$	$1596.58 \pm 75.51$	$268.69 \pm 9.94$	$709.14 \pm 30.23$
tau b-veto	$43.32 \pm 4.25$	$1548.17 \pm 75.28$	$259.86 \pm 9.83$	$700.87 \pm 30.17$
	$Z \rightarrow \tau\tau$	Rare	$t\bar{t}$	$t\bar{t}V$
this region	$1622.59 \pm 34.11$	$3562.03 \pm 21.28$	$54565.58 \pm 86.65$	$150.08 \pm 1.39$
tau b-veto	$1585.45 \pm 33.27$	$3431.48 \pm 20.90$	$52130.19 \pm 84.74$	$143.86 \pm 1.36$
	$\bar{t}t \rightarrow bWcH$	$cg \rightarrow tH$	tcH merged signal	$\bar{t}t \rightarrow bWuH$
this region	$111.46 \pm 0.99$	$6.06 \pm 0.08$	$117.52 \pm 0.99$	$114.44 \pm 0.98$
tau b-veto	$108.10 \pm 0.97$	$5.91 \pm 0.08$	$114.01 \pm 0.98$	$110.93 \pm 0.96$
	$ug \rightarrow tH$	tuH merged signal	Data	
this region	$30.89 \pm 0.41$	$145.33 \pm 1.06$	$57335.00 \pm 239.45$	
tau b-veto	$29.91 \pm 0.40$	$140.84 \pm 1.04$	$54806.00 \pm 234.11$	

Table 7: The cutflow tables in the  $l\tau_{\text{had}} 2j$  signal region.

	SM Higgs	W+jets	Diboson	$Z \rightarrow ll$
this region	$15.04 \pm 2.18$	$945.47 \pm 45.67$	$99.84 \pm 8.34$	$237.32 \pm 21.03$
tau b-veto	$14.31 \pm 2.15$	$908.98 \pm 45.31$	$97.52 \pm 8.33$	$231.64 \pm 20.99$
	$Z \rightarrow \tau\tau$	Rare	$t\bar{t}$	$t\bar{t}V$
this region	$25.37 \pm 3.63$	$356.68 \pm 6.59$	$5402.45 \pm 27.28$	$57.87 \pm 0.71$
tau b-veto	$24.25 \pm 3.60$	$318.29 \pm 6.23$	$4479.10 \pm 24.93$	$54.67 \pm 0.69$
	$\bar{t}t \rightarrow bWcH$	$cg \rightarrow tH$	tcH merged signal	$\bar{t}t \rightarrow bWuH$
this region	$56.24 \pm 0.59$	$1.44 \pm 0.03$	$57.68 \pm 0.59$	$58.60 \pm 0.60$
tau b-veto	$54.47 \pm 0.58$	$1.41 \pm 0.03$	$55.87 \pm 0.58$	$56.81 \pm 0.59$
	$ug \rightarrow tH$	tuH merged signal	Data	
this region	$7.95 \pm 0.17$	$66.55 \pm 0.62$	$7077.00 \pm 84.12$	
tau b-veto	$7.74 \pm 0.17$	$64.55 \pm 0.61$	$6150.00 \pm 78.42$	

Table 8: The cutflow tables in the TTH  $\tau_{\text{lep}}\tau_{\text{had}}$  region.

	SM Higgs	W+jets	Diboson	$Z \rightarrow ll$
this region	$78.09 \pm 3.57$	$949.53 \pm 23.63$	$256.48 \pm 10.66$	$366.66 \pm 12.55$
tau b-veto	$74.43 \pm 3.45$	$922.72 \pm 23.54$	$249.33 \pm 10.59$	$362.06 \pm 12.52$
	$Z \rightarrow \tau\tau$	Rare	$t\bar{t}$	$t\bar{t}V$
this region	$979.60 \pm 14.38$	$1746.76 \pm 14.80$	$40069.19 \pm 73.92$	$293.97 \pm 2.32$
tau b-veto	$942.69 \pm 14.18$	$1677.04 \pm 14.50$	$38188.59 \pm 72.21$	$281.59 \pm 2.27$
	$\bar{t}t \rightarrow bWcH$	$cg \rightarrow tH$	tcH merged signal	$\bar{t}t \rightarrow bWuH$
this region	$143.63 \pm 1.20$	$4.69 \pm 0.07$	$148.32 \pm 1.21$	$150.75 \pm 1.19$
tau b-veto	$138.88 \pm 1.18$	$4.55 \pm 0.07$	$143.44 \pm 1.19$	$145.97 \pm 1.18$
	$ug \rightarrow tH$	tuH merged signal	Data	
this region	$25.91 \pm 0.40$	$176.67 \pm 1.26$	$40395.00 \pm 200.99$	
tau b-veto	$25.18 \pm 0.39$	$171.15 \pm 1.24$	$38458.00 \pm 196.11$	

Table 9: The cutflow tables in the  $l\tau_{\text{had}}\tau_{\text{had}}$  signal region.

	SM Higgs	W+jets	Diboson	$Z \rightarrow ll$
this region	$9.75 \pm 0.20$	$34.72 \pm 14.21$	$16.00 \pm 1.36$	$16.32 \pm 6.83$
tau b-veto	$9.09 \pm 0.20$	$33.79 \pm 14.20$	$14.93 \pm 1.35$	$14.91 \pm 6.72$
	$Z \rightarrow \tau\tau$	Rare	$t\bar{t}$	$t\bar{t}V$
this region	$17.45 \pm 4.85$	$23.67 \pm 1.49$	$322.81 \pm 6.63$	$18.31 \pm 0.42$
tau b-veto	$16.38 \pm 4.81$	$21.81 \pm 1.43$	$253.77 \pm 5.91$	$16.97 \pm 0.41$
	$\bar{t}t \rightarrow bWcH$	$cg \rightarrow tH$	tcH merged signal	$\bar{t}t \rightarrow bWuH$
this region	$61.42 \pm 0.61$	$4.74 \pm 0.06$	$66.16 \pm 0.61$	$63.89 \pm 0.62$
tau b-veto	$57.51 \pm 0.59$	$4.46 \pm 0.06$	$61.97 \pm 0.59$	$60.13 \pm 0.61$
	$ug \rightarrow tH$	tuH merged signal	Data	
this region	$21.93 \pm 0.29$	$85.81 \pm 0.69$	$407.00 \pm 20.17$	
tau b-veto	$20.76 \pm 0.28$	$80.89 \pm 0.67$	$322.00 \pm 17.94$	

## 7 FCNC signal samples

The targeted signal in this analysis is  $tqH/tH$  with  $H \rightarrow \tau\tau$  (samples 411170-411177 and 412098-412105) in App. ??). However, if the FCNC processes exists, the other decays of the Higgs can be part of the signal. Therefore, samples xxxxxx-xxxxxx with inclusive  $W$  and Higgs decays are also included. These sample have a one-lepton (electron or muon) filter at truth level (either coming from  $W$  or Higgs decays). Events overlapping with xxxxxx-xxxxxx are removed based on truth information.

It is checked that after the final selection, there are 110 overlapped signal events caused by different overlap removal and object definition in xTauFramework and ttHMultiAna (27140 in total for hadhad channel and 95253 in total for lepton channels) but there is no overlap in the signal enriched region ( $\text{BDT} > 0.5$ ).

The total FCNC signal with fake taus in this analysis is not used in the MVA training, but is regarded as part of the total signal in the fit. The normalization factor of the other components is common with the signal, so that their yields are fully correlated in the fit.

## 8 Background estimation

The background events with real tau leptons are represented by Monte Carlo (MC) samples. These include  $t\bar{t}$ ,  $t\bar{t}+H/V$  and single top events with real taus, and  $Z \rightarrow \tau\tau$ +jets. The  $Z \rightarrow ee, \mu\mu$  processes are included for lepton faking tau background, and the contribution from jet faking tau. The fake background with one or more taus faked by jets consists of the top fake (with at least one fake tau from jets in the top events), QCD multijet,  $W$ +jets and diboson events. Where the top is dominant as shown in Figure 4.

However, the charge of two taus candidates might be correlated in the  $t\bar{t}$  events when one of taus is a real tau from the  $W \rightarrow \tau\nu$  decay while the other tau is a fake from a jet from other  $W \rightarrow jj$  decay. They are likely to carry the opposite charges to each other. Because of this charge asymmetry we have to calibrate the fake-tau modeling using a Data-Driven (DD) Scale Factor (SF) method by comparing the normalization of fake-tau events in MC to data in the control regions. This SF is then applied to correct the normalization of tau fakes in the MC yields. The excess of the events over these MC background is then from the multi-jets (QCD) faking background.

### 8.1 Origin of fake $\tau_{\text{had}}$

Top fake is the largest fake background in the total fake in the leptonic channels. Within the top fake events, fake taus can come from different origins, i.e., from jets (heavy/light flavor quark or gluon initiated) or leptons (electron or muon). The tau fake origins are checked with the top MC. Three dedicated top pair production control regions are define for:



- W-jet faking tau: exactly 1 lepton, exactly 1 tau candidate, at least 4 jets with exactly 2 b-tagged. Tau candidate and lepton have the same charge.
- B-jet faking tau: 2 leptons with different flavors or away from Z pole ( $M_{ll} > 100\text{GeV}$  or  $M_{ll} < 90\text{GeV}$ ), exactly 1 tau candidate, exactly 1 b-tagged jet.
- Radiation faking tau: 2 leptons with different flavors or away from Z pole, exactly 1 tau candidate, at least two jets with exactly 2 b-tagged jets.

$E_T^{\text{miss}} > 20\text{GeV}$  is required for the top control regions to ensure that QCD contribution is negligible. The detailed categorisation and plots are shown in section 8.2. Most of the fake taus come from quark initiated jets, but the flavor distributions in OS are similar to those in SS.

## 8.2 MC fake $\tau_{\text{had}}$ estimation

As shown in the Figure 4, the data is generally over-estimated in the OS regions while it is opposite in the SS region. If the fake taus are corrected by the same scale factors, this mismodelling will never get solved. This asymmetry of the SS and OS fake taus can be interpreted by the mis-modelling of the fake tau charges. Since the fake taus mainly come from light-flavored jets as shown in Figure 5, the mis-modelling is related to the charge carried by the jets. In conclusion, the mis-modelling is originated from the charge correlation between the jet which is faking a tau and the lepton. So the parent of the jet is believed to be charge correlated with the lepton. Considering the main background is  $\bar{t}t$  process. The only suspect is the hadronic  $W$  boson. In order to find the contribution of w-jet faking taus ( $\tau_W$ ). the truth information is used to match between the w-jet and the fake tau with  $\Delta R < 0.4$ . As shown in the Figure 5, there is a considerable amount of  $\tau_W$ 's in both SS and OS regions. There are four kinds of fake taus that need to be calibrated: Type1)  $\tau_W$ 's with the opposite charge of the lepton; Type2)  $\tau_W$ 's with the same charge of the lepton; Type 3) the fake taus from b-jets; Type4) the fake taus from other origins(mainly radiations). Many control regions are used to calibrate the four types.

- $2l1tau1bnj$ : 2 leptons with different flavors or away from Z pole, exactly 1 tau candidate, exactly 1 b-tagged jets.
- $2l1tau2bnj$ : 2 leptons with different flavors or away from Z pole, exactly 1 tau candidate, exactly 2 b-tagged jets.
- $1l1tau2b2jSS$ : Exactly 1 lepton, exactly 1 tau candidate, exactly 4 jets with exactly 2 b-tagged. Tau candidate and lepton have the same charge.
- $1l1tau2b2jOS$ : Exactly 1 lepton, exactly 1 tau candidate, exactly 4 jets with exactly 2 b-tagged. Tau candidate and lepton have the opposite charge.

Table 10: The scale factors for 1 prong fake taus derived from the fit.

	25 – 35 GeV	35 – 45 GeV	45GeV–
$\tau_{b \text{ fake}}$	$0.61 \pm 0.10$	$0.83 \pm 0.10$	$0.84 \pm 0.07$
$\tau_{other}$	$1.19 \pm 0.02$	$1.00 \pm 0.04$	$0.77 \pm 0.03$
$\tau_{W \text{ OS}}$	$0.67 \pm 0.01$	$0.62 \pm 0.02$	$0.37 \pm 0.02$
$\tau_{W \text{ SS}}$	$0.82 \pm 0.05$	$0.50 \pm 0.07$	$0.74 \pm 0.07$

Table 11: The scale factors for 3 prong fake taus derived from the fit.

	25 – 35 GeV	35 – 45 GeV	45GeV–
$\tau_{b \text{ fake}}$	$1.04 \pm 0.14$	$1.33 \pm 0.13$	$1.22 \pm 0.11$
$\tau_{other}$	$1.24 \pm 0.07$	$0.70 \pm 0.08$	$0.73 \pm 0.08$
$\tau_{W \text{ OS}}$	$0.92 \pm 0.03$	$1.07 \pm 0.04$	$0.21 \pm 0.05$
$\tau_{W \text{ SS}}$	$1.00 \pm 0.10$	$1.07 \pm 0.09$	$0.73 \pm 0.08$

- $1l1\tau2b3jSS$ : Exactly 1 lepton, exactly 1 tau candidate, at least 5 jets with exactly 2 b-tagged. Tau candidate and lepton have the same charge.
- $1l1\tau2b3jOS$ : Exactly 1 lepton, exactly 1 tau candidate, at least 5 jets with exactly 2 b-tagged. Tau candidate and lepton have the opposite charge.

Where di-lep regions ( $2l1\tau1b$  and  $2l1\tau2b$ ) are used to calibrate the Type3 and Type4 fake taus. As explained in the 8.1, these regions are dominated by the bjet and the radiation jet faking taus. 2bOS regions ( $1l1\tau2b2jOS$  and  $1l1\tau2b3jOS$ ) are used to calibrate Type1 fake taus. Compared to the signal region, this region has an additional b-jet. So the  $\bar{t}t$  background is enhanced in this region and signal is depleted. Similarly for the Type2 we can use 2bSS regions ( $1l1\tau2b2jSS$  and  $1l1\tau2b3jSS$ ) to calibrate. The components of these regions are shown in Figure 6. Then a simultaneous fit is made to derive the scale factors for the fake taus. There are four parameters needed to be decided (the scale factors for the 4 types). But considering the  $p_T$  and number of tracks dependence of the tau reconstruction, the scale factors are derived in 3  $p_T$  slices (25-35,35-45,45-inf)GeV and 1/3 prong taus. So there are 24 parameters to be decided. The results is shown in table 10 and 11. All of the CP and theory uncertainties are used to derive the uncertainty of the scale factors. The post-fit plots are shown in Figure 7. Then the scale factors are applied to the corresponding single b-jet regions. In  $l\tau_{had}\tau_{had}$  channel, both taus can be fake, so the calibration is done to them separately, following the same procedure as  $\tau_{lep}\tau_{had}$  channels using the lepton and fake tau charges, then the scale factors are multiplied together.

Table 12: The QCD transfer factor derived from different low  $E_T^{miss}$  control regions

	Electron	Muon
$l\tau_{had}j$ ss	$0.76 \pm 0.19$	$0.57 \pm 0.11$
STH $\tau_{lep}\tau_{had}$ os	$0.60 \pm 0.47$	$1.39 \pm 0.35$
$l\tau_{had}2j$ ss	$0.74 \pm 0.42$	$0.54 \pm 0.23$
TTH $\tau_{lep}\tau_{had}$ os	$1.12 \pm 0.90$	$1.18 \pm 0.52$
Combined	$0.75 \pm 0.18$	$0.64 \pm 0.25$

### 8.3 QCD fake background in $\tau_{lep}\tau_{had}$ and $l\tau_{had}$ regions

After the fake tau calibration, the fake lepton contribution from QCD is also estimated using ABCD method. For each  $\tau_{lep}\tau_{had}$  and  $l\tau_{had}$  signal regions, 4 blocks are defined as follows:

- A:  $E_T^{miss} < 20\text{GeV}$ , PLV not tight
- B:  $E_T^{miss} < 20\text{GeV}$ , PLV tight
- C:  $E_T^{miss} > 20\text{GeV}$ , PLV not tight
- D:  $E_T^{miss} > 20\text{GeV}$ , PLV tight

The transfer factors are measured in each signal region as  $r = \frac{N_B}{N_A}$ . Where  $N_A$  and  $N_B$  are the yields calculated by data-MC where MC includes real lepton background with real taus or calibrated fake taus. The results are shown in 12. The uncertainties in the table for each region contains statistical uncertainties during the calculation and the potential signal contribution ( $BR = 0.2\%$ ). In principle for the QCD estimation, the transfer factor should not depend on the number of jets and charge. At the same time, we see little pt dependence in the CRs. So all of the measurements are taken into consideration and the transfer factor central value and stat uncertainty are derived using likelihood method separately for electron and muons. The systematics variation is taken by calculating the second moment among four regions. The combined result is shown as the last line in the table with both stats and systematics considered, where the stats. uncertainty for electron and muon are 0.13 and 0.07 respectively. So the systematic uncertainties are comparable with the stats uncertainties, which indicates that there is no big deviation among the 4 measurements.

Then the QCD contribution in D is then estimated as  $rC$ . After the ABCD QCD estimation, the signal region is redefined as D. The data-MC comparison after the fake tau and fake lepton estimation is show in Figure 8.

## 8.4 QCD fake $\tau_{\text{had}}$ estimate in $\tau_{\text{had}}\tau_{\text{had}}$

Figure 9 shows the  $\tau_{\text{had}}$   $p_T$  spectra in the  $\tau_{\text{had}}\tau_{\text{had}}$  SS and OS. The fake tau background events from QCD multi-jets is not added yet so the data have more than the background prediction. The top fake are dominated by fakes with one real tau. It is found, based on the MC prediction, that the QCD fake is the dominant fake process in the  $\tau_{\text{had}}\tau_{\text{had}}$  channel.

The excess of the SS events over MC with truth taus are used to estimate the fake tau background in OS from QCD multi-jets in the  $\tau_{\text{had}}\tau_{\text{had}}$  + jets channel:

$$N_{\text{QCD fake}}^{\text{OS}} = f_{\text{norm}} \cdot (N_{\text{data}}^{\text{SS}} - N_{\text{MC}}^{\text{SS}}), \quad (7)$$

where  $f_{\text{norm}}$  is a ratio of OS and SS from multi-jets QCD,  $N_{\text{data}}^{\text{SS}}$ , and  $N_{\text{MC}}^{\text{SS}}$  are observed data and estimated MC predictions in the SS regions.

The  $f_{\text{norm}}$  is measured separately to be  $1.32 \pm 0.03$  in the signal-depleted one  $b$ -tag events with  $BDT < 0.5$  and  $1.6 \pm 0.1$  in the double  $b$ -tagged  $\tau_{\text{had}}\tau_{\text{had}} + \geq 3\text{jets}$  events, which provides a good closure test of QCD fake tau estimation. We take the difference between these two values as a systematics for the method and assign  $f_{\text{norm}} = 1.3 \pm 0.3$  for the analysis.

## 8.5 Fake lepton background

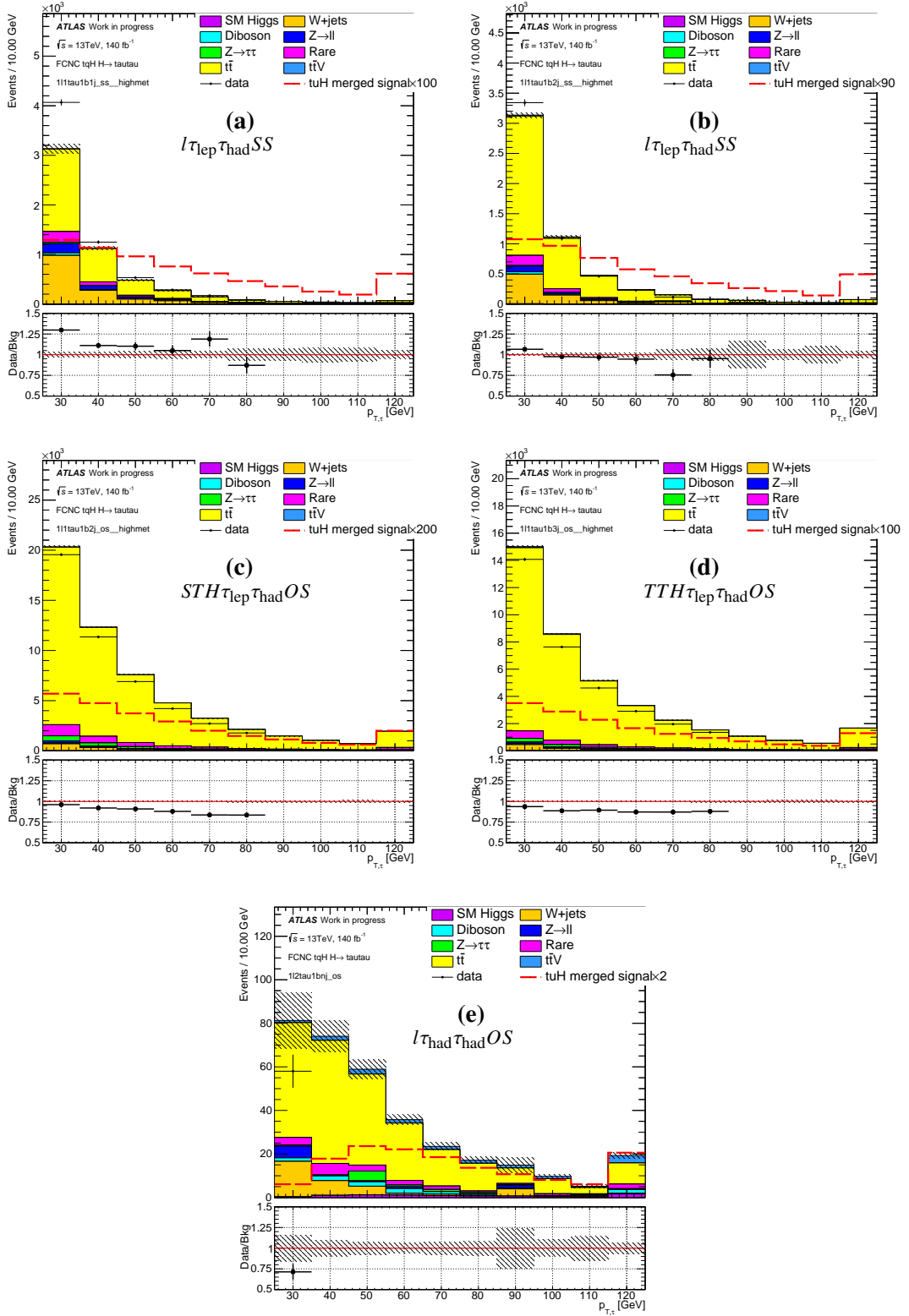
The fake lepton background in  $\tau_{\text{lep}}\tau_{\text{had}}$  and lepton+ $\tau_{\text{had}}\tau_{\text{had}}$ , which is estimated from MC<sup>2</sup>, is about 0.3-0.5% of the total background. It constitutes such a negligible fraction because a very high lepton  $p_T$  threshold is already required at the trigger level. This background is varied by 100% as a conservative systematics.

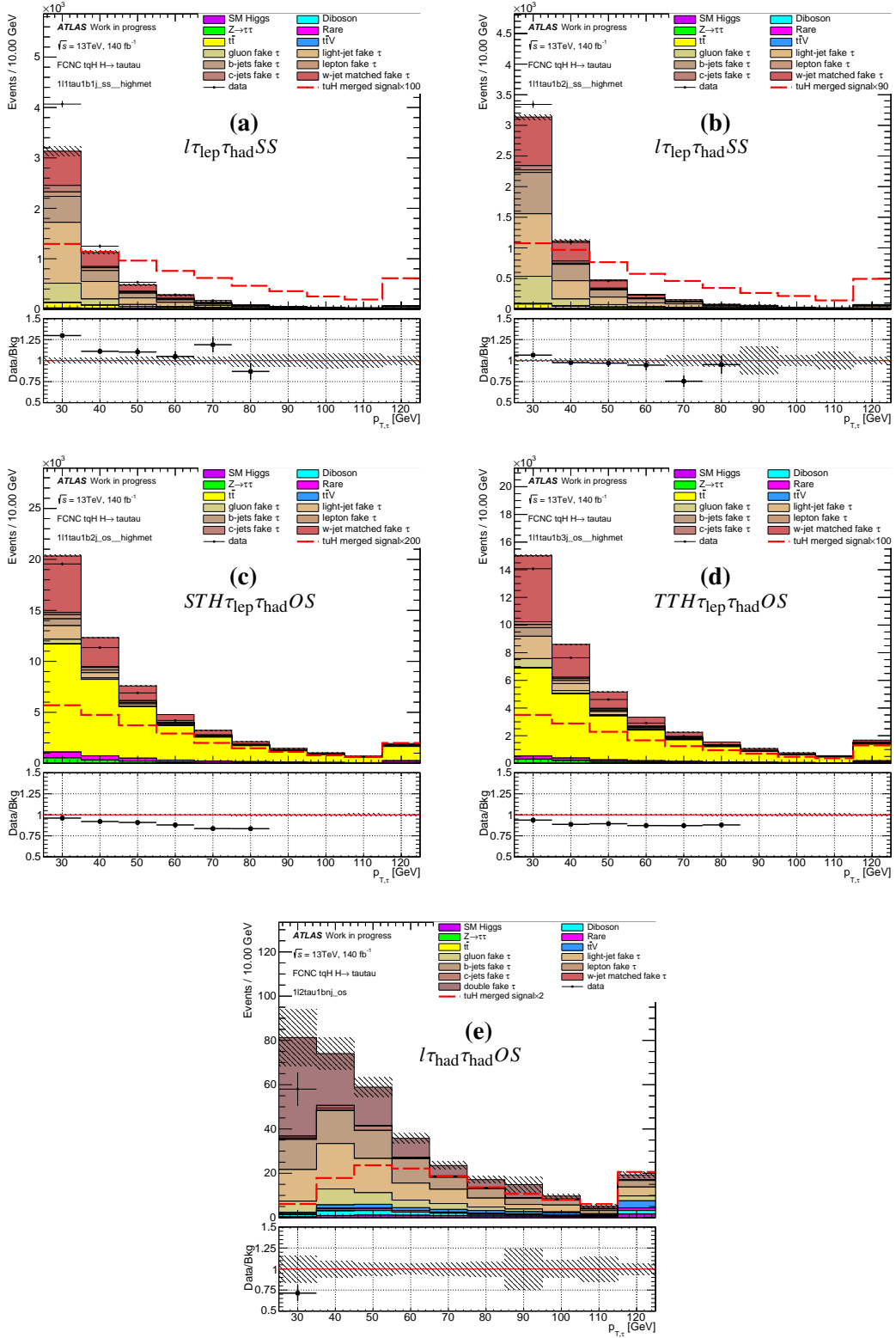
## 8.6 Summary of signal and background events

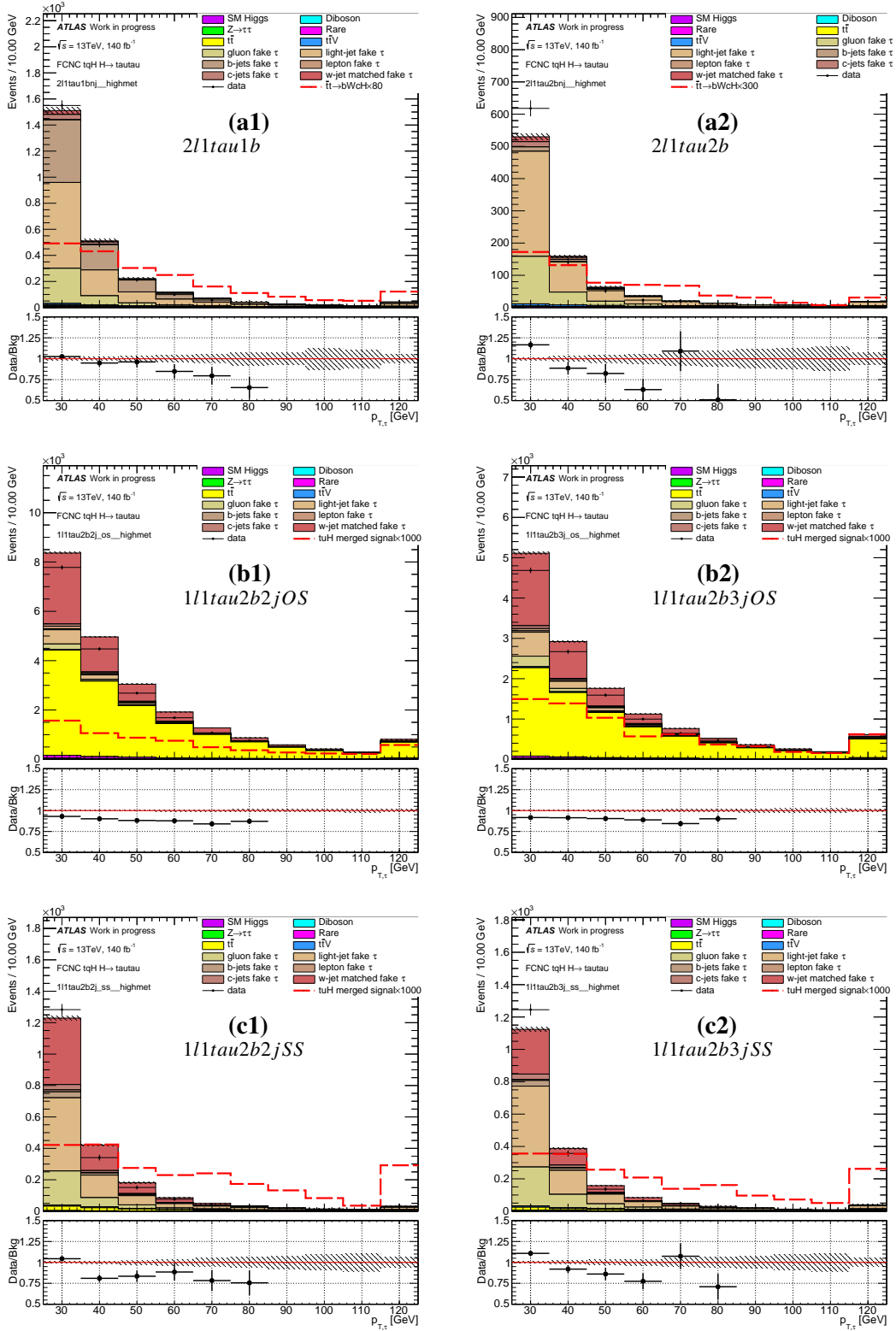
We estimate the expected signal and background events in different regions, which are summarized in Table 14.

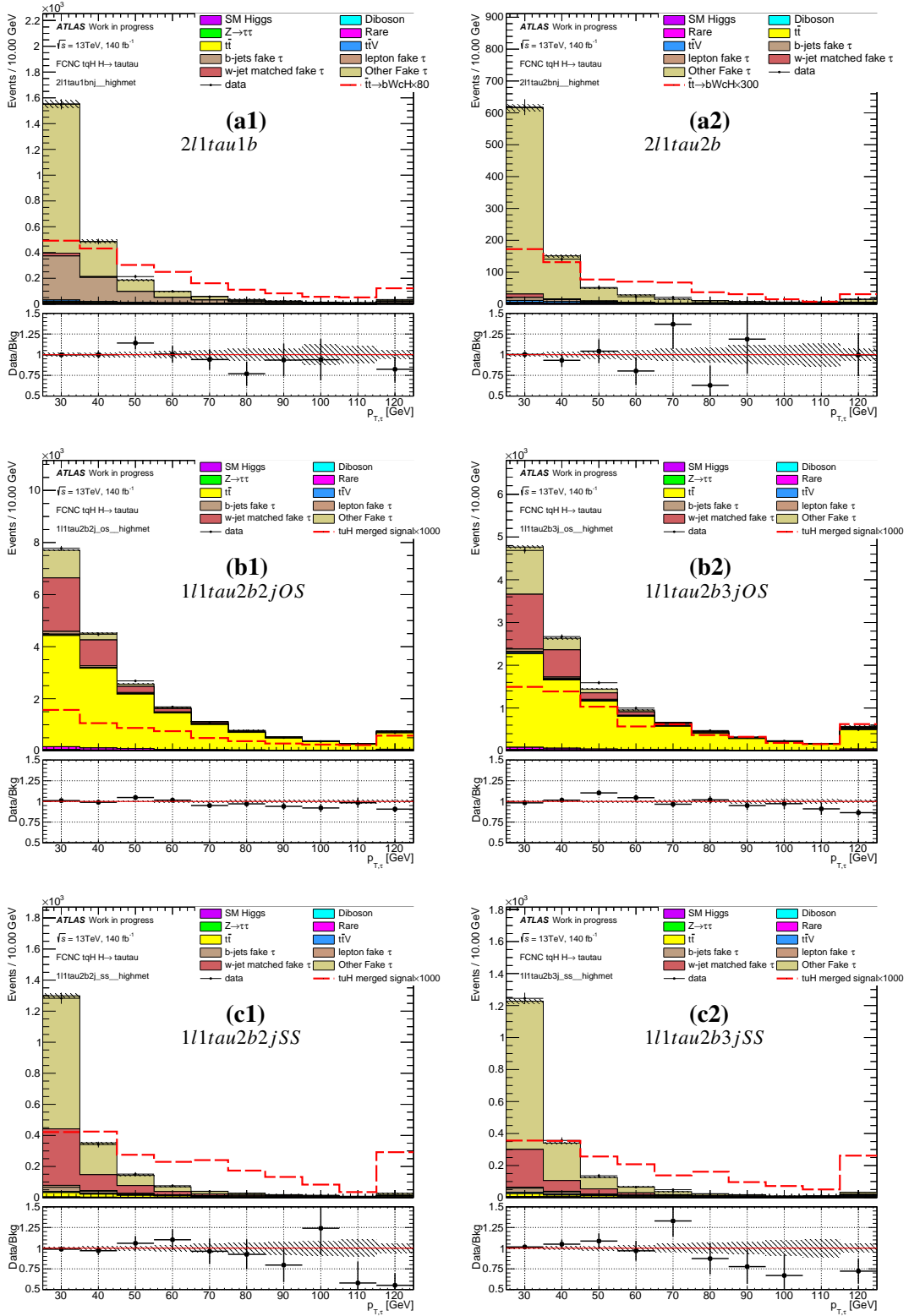
Figure 10 shows the leading  $\tau_{\text{had}}$   $p_T$  distribution from the OS events in the  $\tau_{\text{had}}\tau_{\text{had}}$  signal regions where the points are data and the histograms as the expected various backgrounds.

<sup>2</sup> This includes fake lepton + real tau events from all MC samples, namely, top,  $W/Z$ +jets, diboson

Figure 4: The distributions of  $\tau$   $p_T$  in the signal regions.

Figure 5: The distributions of  $\tau p_T$  in the signal regions with fake tau origin shown.

Figure 6: The distributions of  $\tau p_T$  in the control regions used to calibrate the fake taus.

Figure 7: The post-fit distributions of  $\tau p_T$  in the control regions after the fake tau correction.



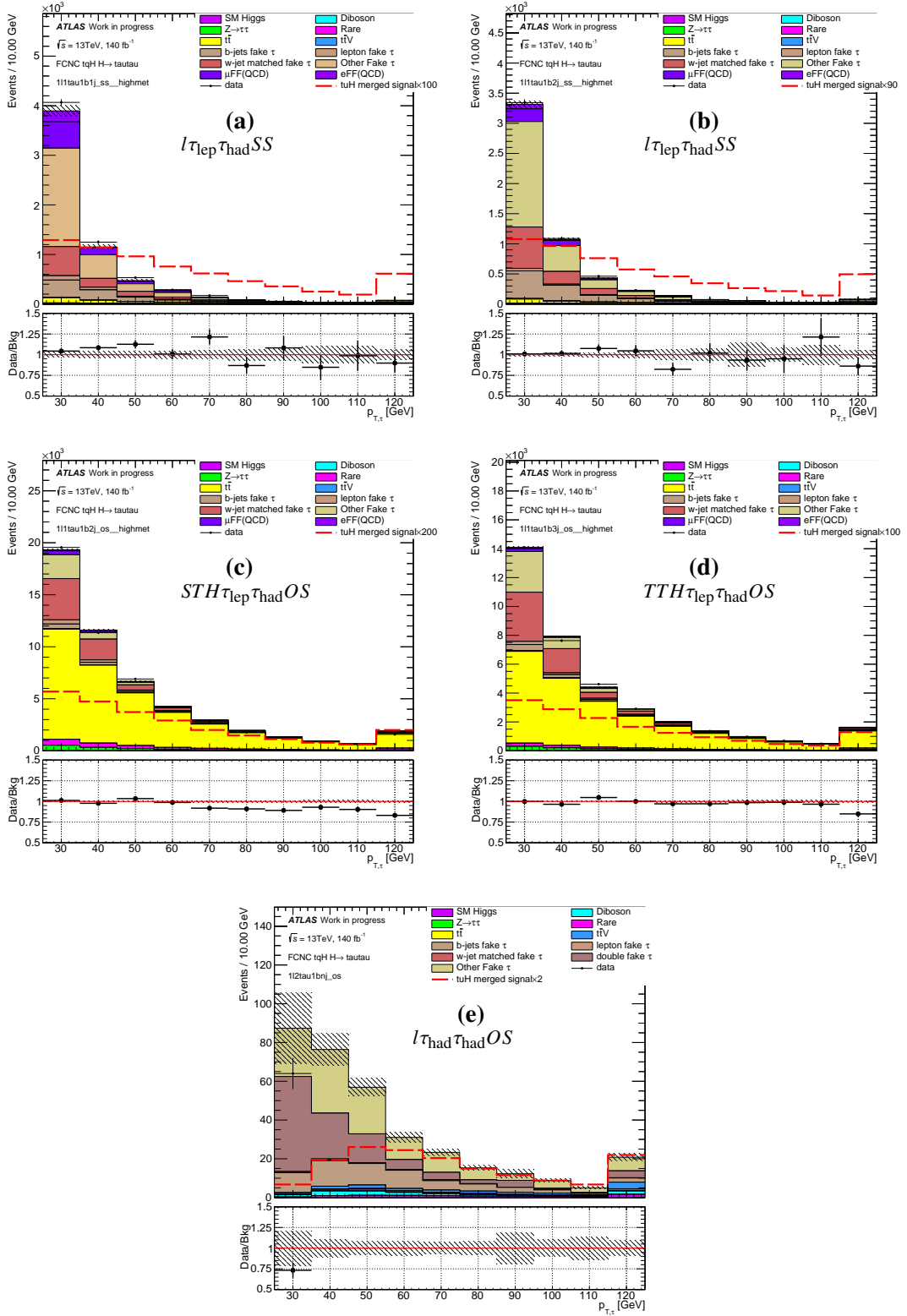


Figure 8: The data-MC comparison of  $\tau p_T$  in the signal regions after the fake tau correction and QCD estimation.

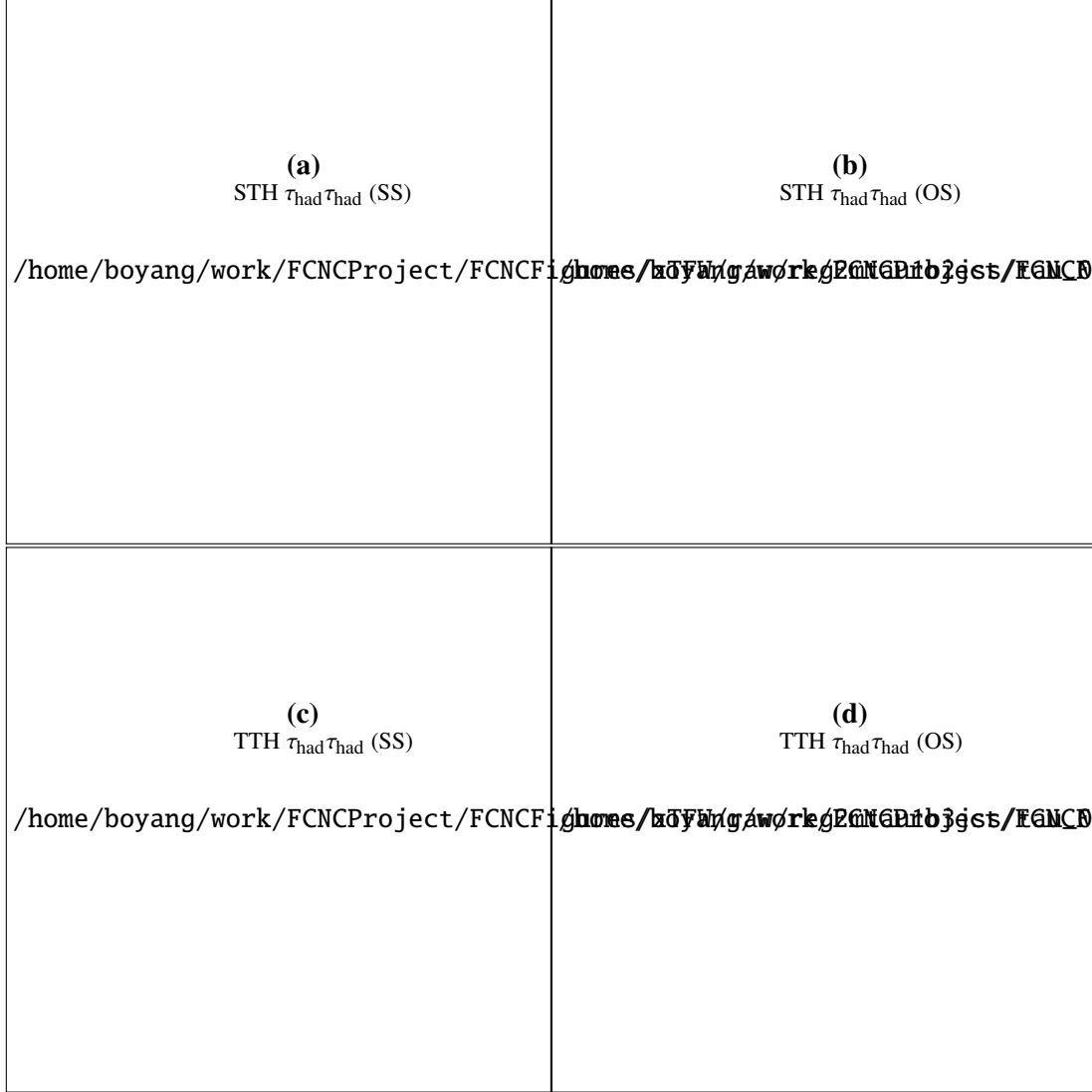


Figure 9: The distributions of  $\tau p_T$  in the STH  $\tau_{\text{had}}\tau_{\text{had}}$  (SS)(a), STH  $\tau_{\text{had}}\tau_{\text{had}}$  (OS) (b), TTH  $\tau_{\text{had}}\tau_{\text{had}}$  (SS) (c) and TTH  $\tau_{\text{had}}\tau_{\text{had}}$  (OS) (d), to illustrate the background composition. Data is more than the prediction because the fake tau backgrounds are missing.

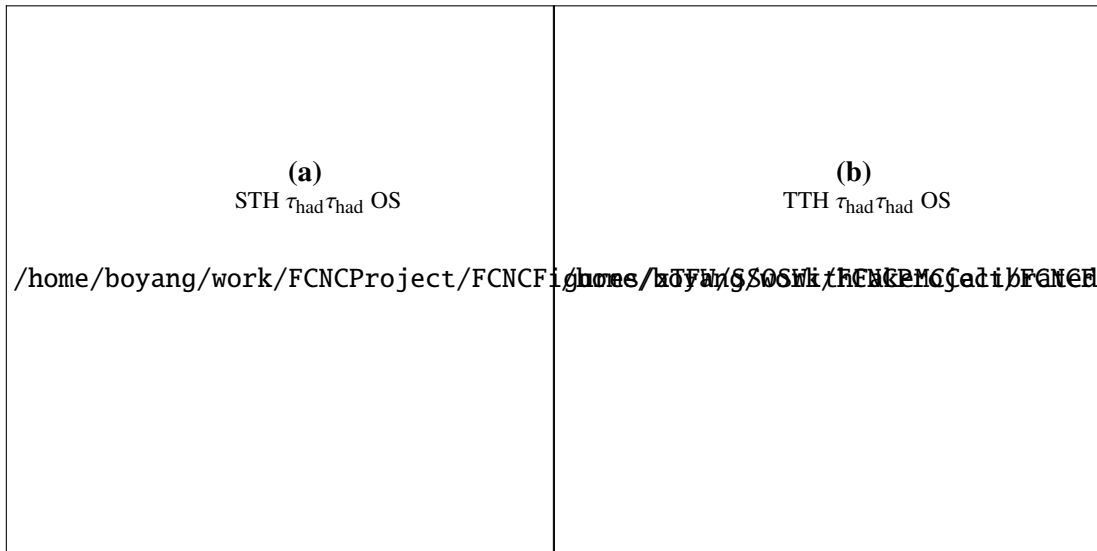


Figure 10: The distributions of leading  $p_T$  in the  $\tau_{had} \tau_{had} + 3$  jets (a), and 4 jets OS (b)

## 9 MVA analysis

In this section, we investigate the sensitivity of probing signal using one of the Multi-Variate Analysis (MVA) methods, the Gradient Boosted Decision Trees (BDT) method [59, 60], with the TMVA software package. The BDT output score is in the range between -1 and 1. The most signal-like events have scores near 1 while the most background-like events have scores near -1.

The signal topology and kinematics are different across all the channels. To maximize the overall sensitivity, separated BDTG trainings are applied to each the signal region. A number of variables as the BDT inputs are used to train and test events in each signal region for maximal signal acceptance and background rejection. They are listed in Tab. ???. The most sensitive variables distributions are shown in Fig. 11-13

The signal and background samples are randomly divided into two equal parts (denoted as even and odd parity events). The BDT is trained with one part, and tested on the other part. It is always ensured that the BDT derived from the training events is not applied to the same events, but only to the independent test ones. The sum of MC all background processes, corrected normalized, are used in the training and testing. With the IgnoreNegWeightsInTraining option, only MC events with positive MC weights are used in the training. The comparison of BDT performances in test-odd and test-even samples is given in Fig. 14-16. The BDT parameters NTrees and nCuts are tuned such that the test-odd and test-even agrees, and the signal sensitivity is optimised.

The importance factors<sup>3</sup> of different variables used in the training is listed in Tab. ??. The two numbers in each block represent the importance factor of the two models trained from even and odd parts. The consistency of these factors implies that the training models are stable.

As a cross check, the comparisons between BDT distributions in testing samples, as well as the test even and test odd ROC curves, are shown in Fig. 14 and 15.

The final yield and stats only significance is shown in Table 14 and Table 15

---

<sup>3</sup> The importance is evaluated as the total separation gain that this variable had in the decision trees (weighted by the number of events). It is normalized to all variables together, which have an importance of 1.

Table 13: The importance (in %) of each variables used in the BDTG training, the two numbers in the each block are from the two training folds.

	$l\tau_{\text{had}}j$ ss	STH $\tau_{\text{lep}}\tau_{\text{had}}$ OS	$l\tau_{\text{had}}2j$ ss	TTH $\tau_{\text{lep}}\tau_{\text{had}}$ OS	$l\tau_{\text{had}}\tau_{\text{had}}$ OS
$p_{T,\tau}$	19.59 / 17.68	8.23 / 7.95	13.37 / 13.70	7.66 / 7.97	6.72 / 8.40
$E_{\text{miss}}^T$	7.83 / 9.26	6.91 / 6.34	4.64 / 3.58	7.59 / 7.32	5.87 / 7.05
$m_{\tau\tau,\text{vis}}$	7.00 / 7.01	8.68 / 9.00	2.32 / 3.75	9.19 / 9.36	13.23 / 11.76
$\Delta R(\tau, \text{light jet}, \min)$	15.88 / 15.37	7.20 / 7.40	9.76 / 10.27	6.88 / 6.37	7.16 / 8.36
$\Delta R(l, b \text{ jet})$	17.01 / 18.42	4.69 / 6.24	12.88 / 12.30	6.30 / 4.87	6.03 / 6.74
$\Delta R(l, \tau)$	14.56 / 11.39	7.93 / 8.17	7.06 / 7.33	7.89 / 7.71	2.92 / 2.47
$\Delta R(\tau, b \text{ jet})$	12.73 / 12.95	7.50 / 6.50	7.12 / 8.37	5.48 / 5.31	4.99 / 2.33
$p_{T,l}$	5.40 / 7.92	3.62 / 3.74	5.86 / 7.20	2.28 / 3.13	1.55 / 2.78
$\Delta\phi(\tau\tau, P_{\text{miss}}^T)$	/	6.55 / 5.28	4.02 / 3.57	5.76 / 5.08	/
$E_{\text{miss}}^T \text{ centrality}$	/	6.62 / 6.02	4.03 / 4.97	5.14 / 5.72	/
$m_{\tau,\tau}$	/	4.20 / 4.01	1.90 / 2.40	2.94 / 3.64	/
$E_{\nu,1}/E_{\tau,1}$	/	9.75 / 10.16	9.55 / 9.12	8.51 / 9.81	/
$E_{\nu,2}/E_{\tau,2}$	/	8.38 / 9.14	8.02 / 9.85	8.41 / 8.39	/
$m_{t,SM}$	/	5.56 / 5.64	3.37 / 0.79	4.50 / 4.60	/
$M(\text{light jet}, \text{light jet}, \min)$	/	4.19 / 4.39	6.11 / 2.80	5.65 / 4.86	/
$m_W$	/	/	/	3.28 / 3.27	/
$\chi^2$	/	/	/	2.55 / 2.58	/
$\Delta R(\tau, \tau)$	/	/	/	/	9.19 / 9.45
$m_{t,SM,\text{vis}}$	/	/	/	/	8.70 / 7.74
$M(\tau \text{light jet}, \min)$	/	/	/	/	4.94 / 1.57
$\eta_{\tau,\text{max}}$	/	/	/	/	6.26 / 6.03
$m_W^T$	/	/	/	/	2.94 / 6.74
$\Delta R(l + b \text{ jet}, \tau + \tau)$	/	/	/	/	6.71 / 8.06
$P_{t,\tau\tau,\text{vis}}$	/	/	/	/	5.61 / 4.78
$m_{t,FCNC,\text{vis}}$	/	/	/	/	7.19 / 5.75

Table 14: The yield of the background, data and each signal before the final fit.

	$l\tau_{\text{had}} 1j$	STH $\tau_{\text{lep}}\tau_{\text{had}}$	$l\tau_{\text{had}} 2j$
data	$6566.00 \pm 81.03$	$50780.00 \pm 225.34$	$5490.00 \pm 74.09$
background	$6226.42 \pm 123.87$	$51650.01 \pm 129.16$	$5436.79 \pm 58.67$
$\bar{t}t \rightarrow bWcH$	$53.79 \pm 0.57$	$95.89 \pm 0.91$	$49.40 \pm 0.55$
$cg \rightarrow tH$	$2.09 \pm 0.04$	$5.25 \pm 0.07$	$1.29 \pm 0.03$
tcH merged signal	$55.88 \pm 0.57$	$101.14 \pm 0.91$	$50.69 \pm 0.55$
$\bar{t}t \rightarrow bWuH$	$55.75 \pm 0.58$	$98.45 \pm 0.90$	$51.77 \pm 0.56$
$ug \rightarrow tH$	$10.62 \pm 0.20$	$26.90 \pm 0.38$	$7.01 \pm 0.16$
tuH merged signal	$66.37 \pm 0.62$	$125.34 \pm 0.98$	$58.78 \pm 0.58$

	TTH $\tau_{\text{lep}}\tau_{\text{had}}$ OS	$l\tau_{\text{had}}\tau_{\text{had}}$ OS
data	$36076.00 \pm 189.94$	$322.00 \pm 17.94$
background	$36535.54 \pm 88.63$	$337.43 \pm 21.16$
$\bar{t}t \rightarrow bWcH$	$123.95 \pm 1.11$	$57.26 \pm 0.59$
$cg \rightarrow tH$	$4.16 \pm 0.07$	$4.45 \pm 0.06$
tcH merged signal	$128.11 \pm 1.11$	$61.71 \pm 0.59$
$\bar{t}t \rightarrow bWuH$	$129.95 \pm 1.10$	$59.88 \pm 0.60$
$ug \rightarrow tH$	$23.35 \pm 0.38$	$20.67 \pm 0.28$
tuH merged signal	$153.31 \pm 1.17$	$80.55 \pm 0.66$

Table 15: The stat. only significance of signal before the final fit.

	$l\tau_{\text{had}} 1j$	STH $\tau_{\text{lep}}\tau_{\text{had}}$	$l\tau_{\text{had}} 2j$
$\bar{t}t \rightarrow bWcH$	1.34	0.74	1.28
$cg \rightarrow tH$	0.05	0.06	0.03
tcH merged signal	1.39	0.80	1.31
$\bar{t}t \rightarrow bWuH$	1.43	0.76	1.38
$ug \rightarrow tH$	0.29	0.39	0.22
tuH merged signal	1.71	1.12	1.59

	TTH $\tau_{\text{lep}}\tau_{\text{had}}$ OS	$l\tau_{\text{had}}\tau_{\text{had}}$ OS
$\bar{t}t \rightarrow bWcH$	1.55	6.08
$cg \rightarrow tH$	0.07	0.58
tcH merged signal	1.62	6.48
$\bar{t}t \rightarrow bWuH$	1.65	6.47
$ug \rightarrow tH$	0.40	2.43
tuH merged signal	2.04	8.26

(a1)  
/home/boyang/work/FCNCProj

(b1)  
/home/boyang/work/FCNCProj

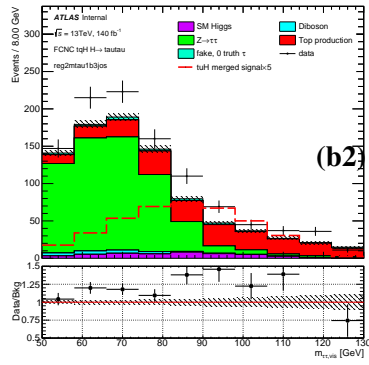
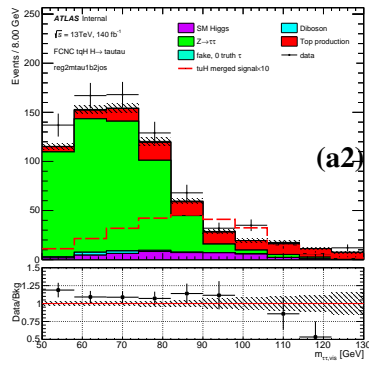


Figure 11: The BDT input distributions for the background and merged signal in the STH  $\tau_{\text{had}}\tau_{\text{had}}$  (a1-3), TTH  $\tau_{\text{had}}\tau_{\text{had}}$  (b1-3)

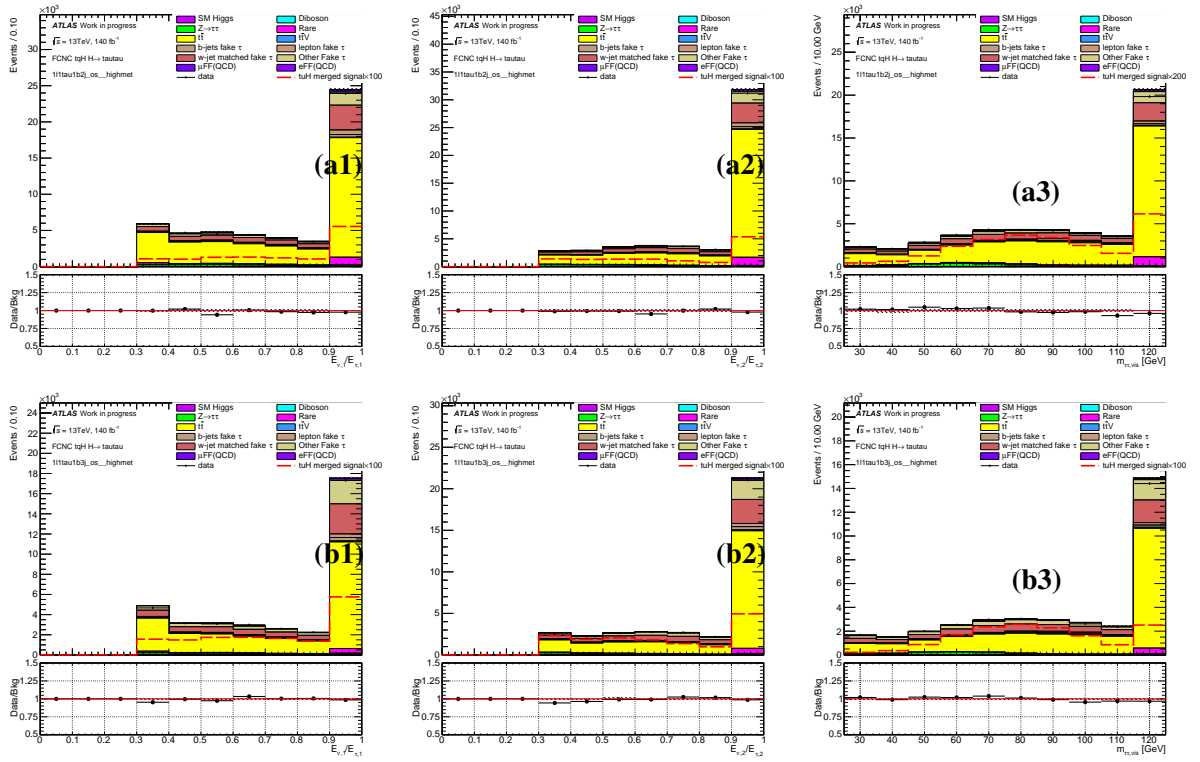


Figure 12: The BDT input distributions for the background and merged signal in the STH  $\tau_{\text{lep}}\tau_{\text{had}}$  (a1-3), TTH  $\tau_{\text{lep}}\tau_{\text{had}}$  (b1-3).



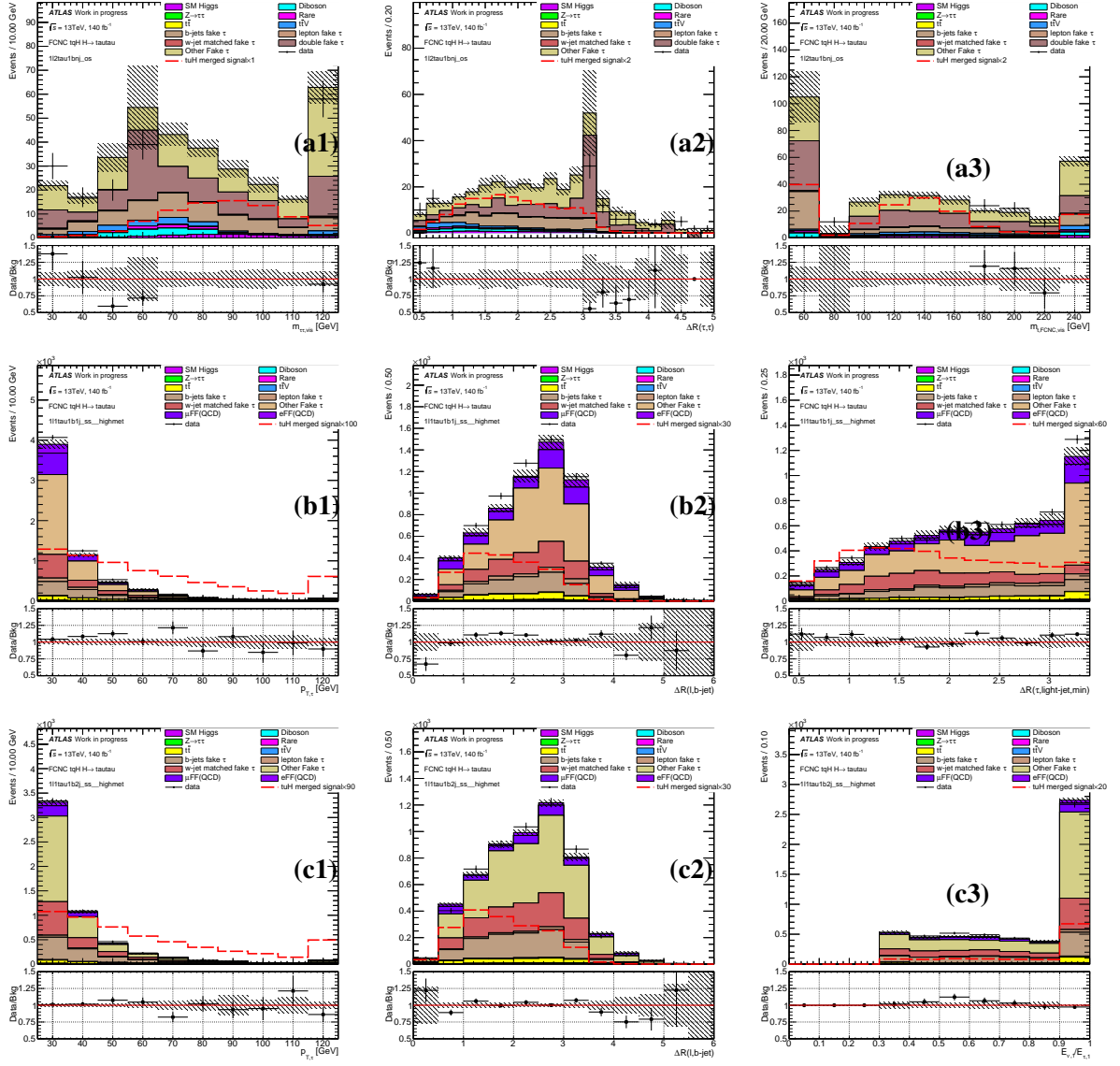


Figure 13: The BDT input distributions for the background and merged signal in the  $l\tau_{\text{had}}\tau_{\text{had}}$  (a1-3),  $l\tau_{\text{had}} 1j$  (b1-3),  $l\tau_{\text{had}}\tau_{\text{had}} 2j$  (c1-3) channels.

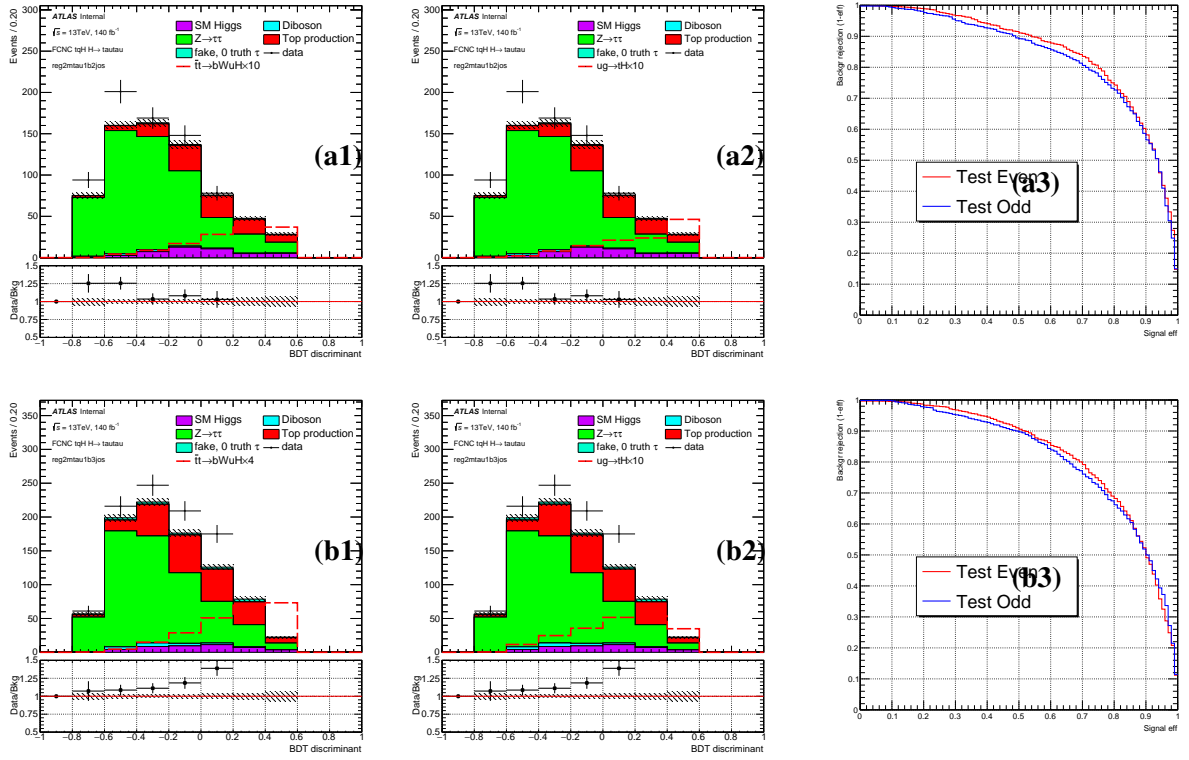


Figure 14: The BDT output distributions for the background and TT signal (a1, b1), background and ST signal (a2, b2) and ROC curves (a3, b3) in the STH  $\tau_{\text{had}}\tau_{\text{had}}$  (a1-3), TTH  $\tau_{\text{had}}\tau_{\text{had}}$  (b1-3).

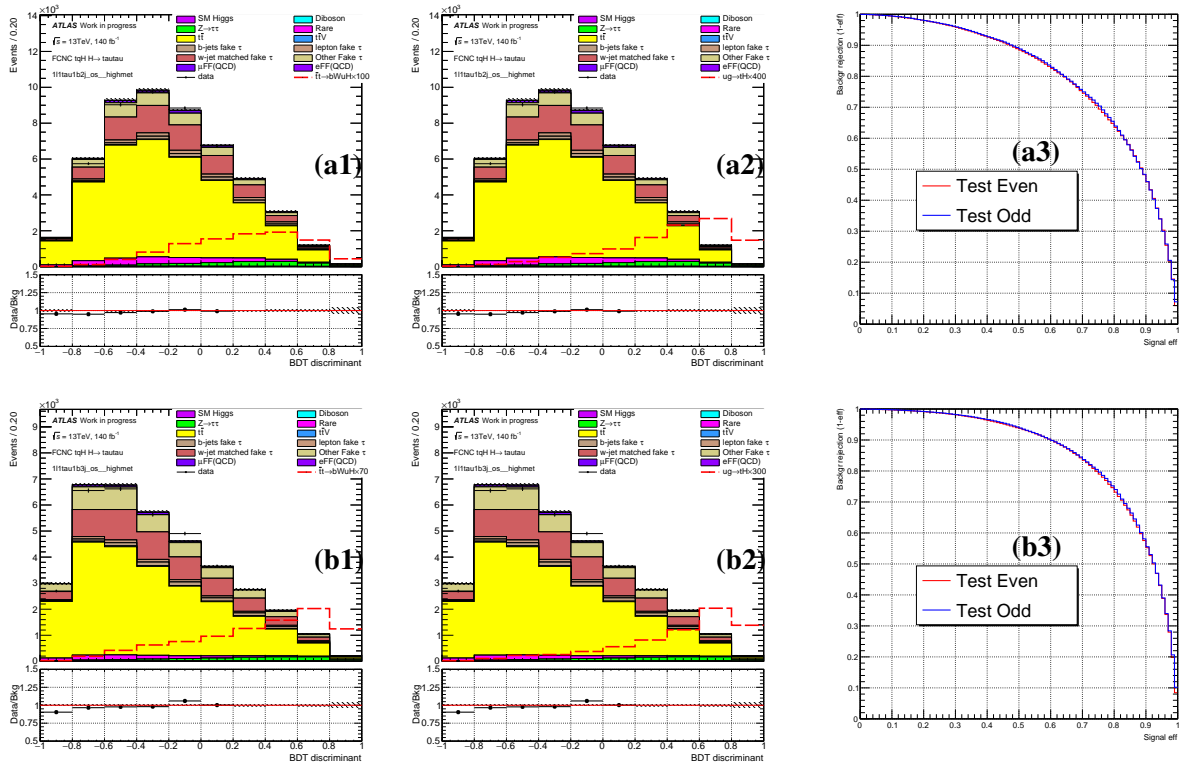


Figure 15: The BDT output distributions for the background and TT signal (a1, b1), background and ST signal (a2, b2) and ROC curves (a3, b3) in the STH  $\tau_{\text{lep}}\tau_{\text{had}}$  (a1-3), TTH  $\tau_{\text{lep}}\tau_{\text{had}}$  (b1-3).

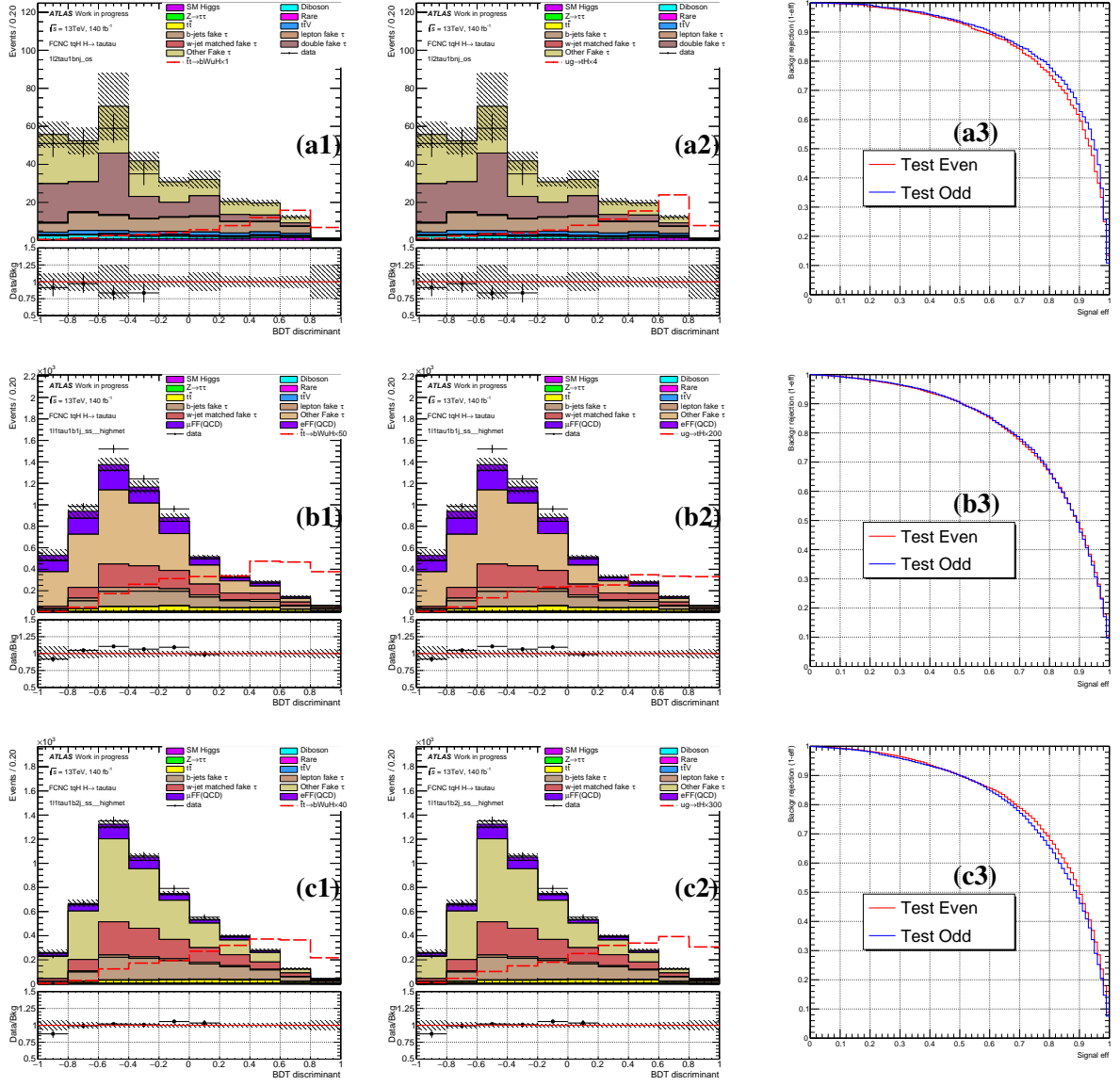


Figure 16: The BDT output distributions for the background and TT signal (a1, b1, c1), background and ST signal (a2, b2, c2) and ROC curves (a3, b3, c3) in the  $l\tau_{\text{had}}\tau_{\text{had}}$  (a1-3),  $\tau_{\text{had}} 1j$  (b1-3),  $\tau_{\text{had}} 2j$  (c1-3) channels.

## 10 Systematic uncertainties

The signal efficiency and the background estimations are affected by uncertainties associated with the detector simulation, the signal modelling and the data-driven background determination. In the combined fit, these uncertainties are called Nuisance Parameters (NP), as opposed to the parameter of interest, the signal strength, which is a scaling factor applied on the total signal events.

Any systematic effect on the the overall normalisation or shape of the final BDT distribution in the signal region is considered. In TRExFitter [61], the NP pruning is applied, which means that NPs whose impact are less than a certain threshold are discarded. The lower thresholds to remove a shape systematic and a normalisation systematic from the fit are both 1% in the fit.

Table ?? gives the QCD fake estimation for  $\tau_{\text{had}}\tau_{\text{had}}$  channel in 8.4 and 24 scale factor NPs and 2 transfer factor for fake method mentioned in 8.2. The lists of systematic NPs that survive the pruning are in Tab. ?? and ??, and their meanings are given below. All the NPs in Tab. ?? and the fake method NP in ?? are fully correlated in all signal regions.

### 10.1 Luminosity

The integrated luminosity measurement has an uncertainty of 1.7% for the combined Run-2 data, and it is applied to all simulated event samples.

### 10.2 Detector-related uncertainties

Uncertainties related to the detector are included for the signal and backgrounds that are estimated using simulation. These uncertainties are also taken into account for the simulated events that enter the data-driven background estimations. All instrumental systematic uncertainties arising from the reconstruction, identification and energy scale of electrons, muons, ( $b$ -)jets and the soft term of the  $E_{\text{T}}^{\text{miss}}$  measurement are considered. The effect of the energy scale uncertainties on the objects is propagated to the  $E_{\text{T}}^{\text{miss}}$  calculation. These systematics include uncertainty associated with:

- The electron and muon trigger, reconstruction, identification and isolation efficiencies. These are estimated with the tag-and-probe method on the  $Z \rightarrow ll$ ,  $J/\psi \rightarrow ll$  and  $W \rightarrow l\nu$  events [62].
- Electron and muon momentum scales. They are estimated from the early 13 TeV  $Z \rightarrow ll$  events.

- Jet energy scale (JES) and resolution (JER). The JES uncertainty is estimated by varying the jet energies according to the uncertainties derived from simulation and in-situ calibration measurements using a model with a reduced set of 38 orthogonal NPs [63] which has up to 30% correlation losses, which are assumed to be uncorrelated, and the induced changes can be added in quadrature. The individual scale variations on the jets are parameterised in  $p_T$  and  $\eta$ . The total JES uncertainty is below 5% for most jets and below 1% for central jets with  $p_T$  between 300 GeV and 2 TeV. The difference between the JER in data and MC is represented by one NP. It is applied on the MC by smearing the jet  $p_T$  within the prescribed uncertainty. JVT is applied in the analysis to select jets from hard-scattered vertices. It was found that different MC generators (and different fragmentation models) lead to efficiency differences of up to 1%, and the uncertainty on the efficiency measurement was found to be around 0.5%. Two NPs are assigned for the JVT efficiency, one for the central and the other for the forward jets.
- Calibration of the  $E_T^{\text{miss}}$ . The uncertainties on  $E_T^{\text{miss}}$  due to systematic shifts in the corrections for leptons and jets are accounted for in a fully correlated way in their evaluation for those physics objects, and are therefore not considered independently here. The systematic uncertainty assigned to the track-based soft term used in the  $E_T^{\text{miss}}$  definition quantifies the resolution and scale of the soft term measurement by using the balance between hard and soft contributions in  $Z \rightarrow \mu\mu$  events. The uncertainties are studied using the differences between Monte Carlo generators, using Powheg+Pythia8 as the nominal generator [64]. One NP is assigned for the soft-track scale, and two NPs for the soft-track resolution.
- Jet flavour tagging systematics. The uncertainties on the  $b$ -tagging are assessed independently for  $b$ ,  $c$  and light-flavour quark jets, with extrapolation factors [65]. The efficiencies and mis-tag rates are measured in data using the methods described in [66]-[67] with the 2015, 2016 and 2017 data set. There are 19 NPs assigned for the flavour tagging systematics (so-called “Loose” reduced set, with 5 NPs for light flavor, 4 for  $c$ , 9 for  $b$ , and 1 for extrapolation).
- Pileup. The uncertainty on the pileup reweighting is evaluated by varying the pileup scale factors by  $1\sigma$  based on the reweighting of the average interactions per bunch crossing. However, this uncertainty is highly correlated with the luminosity uncertainty and may be an overestimate.
- Tau object systematics. These include the  $\tau_{\text{had}}$  reconstruction, identification and trigger efficiencies, the efficiency for tau-electron overlap removal of true  $\tau_{\text{had}}$ , the one for tau-electron overlap removal of true electrons faking  $\tau_{\text{had}}$ , and the one for a “medium” BDT electron rejection. There are also three NPs that cover the tau energy scale (TES) systematics due to the modeling of the detector geometry (TAU\_TES\_DETECTOR), the measurement in the tag-and-probe analysis (TAU\_TES\_INSITU) and the Geant4 shower model (TAU\_TES\_MODEL). The systematics are based on detailed MC variation study, as well as the Run-2  $Z \rightarrow \tau\tau$  data for insitu calibrations of the tau TES and trigger efficiencies, as documented in [51] and the dedicated software tools [53] recommended by the Tau CP Working Group [54].

### 10.3 Uncertainties on fake background estimations

Systematic uncertainties resulting from the data-driven background estimation and usage of SS events as described in Sec. 8. They are named `fakeSF*prong*Ptb` and `norm_factor_hh` in Tab. ??.

### 10.4 Theoretical uncertainties on the background

Theoretical uncertainties have been applied to the MC background in this analysis. The NNPDF3.0 systematic set (which has 100 variations) is used to get the variation envelope around the nominal PDF, and the renormalization and factorization scales are varied by a factor of 0.5 and 2.0 around the nominal values. There are eight such variations. In the final BDT distributions, the largest variations of the eight per bin are taken.

The default  $t\bar{t}$  sample is generated with Powheg. A separate full-sim  $t\bar{t}$  sample generated with Sherpa (0 and 1-jet at NLO, and  $\geq 2$  jets at LO) is compared with the Powheg sample, and the difference in final results is treated as the hard scattering systematics [68].

The default  $t\bar{t}$  MC events are showered with Pythia8. A separate sample showered with Herwig7 is compared with the Pythia8 sample, and the difference is treated as fragmentation and hadronization systematics [68]. These two samples are both generated with ATLFast-II [36], and their difference is then applied to the default full-simulation  $t\bar{t}$  sample.

The Powheg+Pythia8  $t\bar{t}$  MC is also generated with different shower radiations (initial and final-state radiation modelling). For a sample with increased radiation, the factorisation and renormalization scales are scaled by 0.5 with respect to their nominal values, the `hdamp` parameter (which controls the amount of radiation produced by the parton shower in POWHEG-BOX v2) is set to  $3m_{\text{top}}$  and the `A14var3cUp` tune is used. Conversely, for a sample with decreased radiation, the two scales are scaled by 2 with respect to their nominal values, the `hdamp` is kept at the nominal value of  $1.5m_{\text{top}}$  and the `A14var3cDown` tune is used [68].

Uncertainty affecting the normalisation of the  $V$ +jets background is estimated to be about 30% according to the study done in the FCNC  $H \rightarrow b\bar{b}$  channel [69]. The uncertainty on the diboson cross section is 5% [70], on single top +5%/−4% [43][71, 72], on  $t\bar{t}V$  15% [73, 74], and on  $t\bar{t}H$  +10%/−13% [75].

### 10.5 Uncertainties on the signal modelling

Since the signal samples share the same production as the  $t\bar{t}$  process, the systematics listed above for  $t\bar{t}$  also apply to the signal. However, because the systematics variation samples are only generated for the

638 SM decays of  $t\bar{t}$ , only the integral change of the yields observed for the  $t\bar{t}$  background with real taus in  
639 the FR is used, and applied on the signal in the same region in a fully correlated way. An additional 1.6%  
640 uncertainty on  $\text{BR}(H \rightarrow \tau\tau)$  is also assigned [39].

641 The fake calibration is also applied to the fake tau part of the signal the same way as the background. The  
642 6 NPs are also applied to the signal and fully correlated with the background.



## 11 Fit model and signal extraction

The parameter of interest in this search is the signal strength of the FCNC interactions,  $BR(t \rightarrow Hq)$  and corresponding production mode cross section. The statistical analysis of the data employs a binned likelihood function constructed as the product of Poisson probability terms, in bins of the BDT output.

To take into account the systematic uncertainties associated with the MC estimation from different sources for both the signal and background samples, the fit model incorporates these systematics as extra Gaussian or Log-Normal constraint terms multiplied with the combined likelihood. The fitted central values and errors of the systematics parameters, or NPs, are expected to follow a normal distribution centered around 0 with unit width, when the Asimov data is used. The fit model construction is obtained with the `RooFit` and `RooStats` software, and the model configuration and persistence files (as input to `RooStats`) are produced by `TRExFitter` [61], which is a software package interface with `HistFactory`. The `TRExFitter` includes additional features such as histogram smoothing, NP pruning and error symmetrization before the fits.

The correlated bin-by-bin histogram variation corresponds to the up and down variation of each NP. The independent bin-by-bin fluctuations in the combined MC templates are also treated as NPs. They are incorporated in the model as extra Poisson constraint terms, and are expected to have a fitted value of 1 and a fitted error reflecting the relative statistical error in each particular bin. There is one parameter of interest (POI) freely floating in the fit without any constraints, namely, the signal strength  $\mu$  (`SigXsecOverSM`) which is a multiplicative factor on a presumed branching ratio of  $BR(t \rightarrow Hq)=0.2\%$  in this analysis. The errors associated with the different systematics will be properly propagated to the fitted error of  $\mu$  in a simultaneous fit of multiple regions via a profiled likelihood scan by the minimization program `MINUIT`.

The one-sided NPs in the analysis, namely, `fakeSFXprongXPtbin`, `ttbar fragmentation`, `ttbar hard scattering`, `JET_BJES_Response`, `JET_JER_DataVsMC_MC16`, `JET_SingleParticle_HighPt`, `JET_TILECORR_Uncertainty`, `MET_SoftTrk_ResoPara`, `MET_SoftTrk_ResoPerp` are symmetrized. This is done manually on the MC components of the background. By default, all the kinematic NPs (shape NPs due to, e.g., energy scales) are smoothed using the default smoothing parameters in `TRExFitter`. This helps removing the artificial NP constraints due to statistical fluctuations in the systematic variations, and makes the fit well behaved. The NPs pull distributions before the smoothing for each SR are given in App. ??.

Figure 20 shows the ranking of the 25 top NPs along with their pull distributions, produced also with `TRExFitter`. The highest ranked NP is defined to have the largest impact on  $\mu$ . The impact is evaluated by varying the NP under consideration by one  $\sigma$  (either pre or post-fit error) up and down, and afterwards looking at the relative change in  $\mu$  under the conditional fit where the NP under consideration is fixed to its varied new value. Figure ?? shows the pull distributions of all NPs in asimov fit. Normalization and

677 shape systematics whose impact is less than 1% are removed from the fit. The list of removed NPs are  
678 given in App. ??.

679 The NP ranking and constraints can be qualitatively understood from the variations of the BDT distributions  
680 due to the relevant NPs. Figures ??-?? show the systematic variations due to the top ranked NPs.

681 Figure 21 shows the correlation matrix for different NPs. Except for self-correlations, and the correlations  
682 between the normalization factors (including POI) and the others, all the NPs have relatively small  
683 correlations with each other, which justifies the fit models for independent systematics.

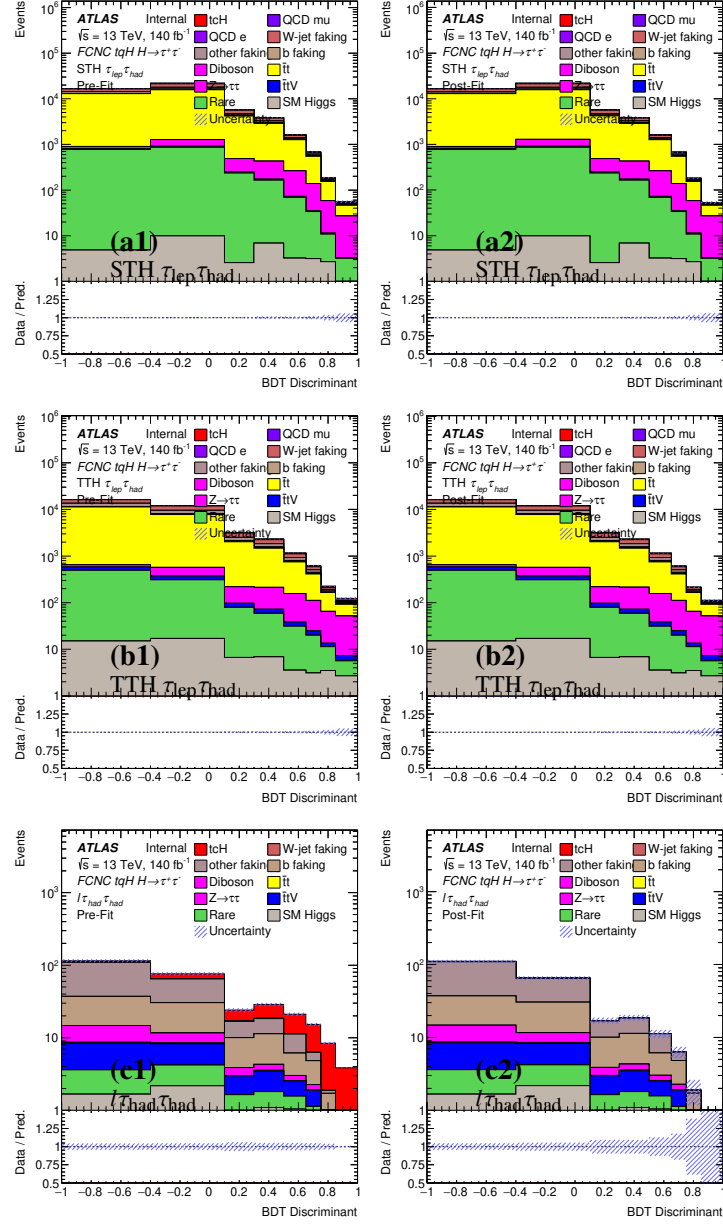


Figure 17: The asimov prefit (left) and postfit (right) BDT distributions in the STH  $\tau_{\text{lep}}\tau_{\text{had}}$  (a1-2) and TTH  $\tau_{\text{lep}}\tau_{\text{had}}$  (b1-2),  $t\tau_{\text{had}}\tau_{\text{had}}$  (c1-2)

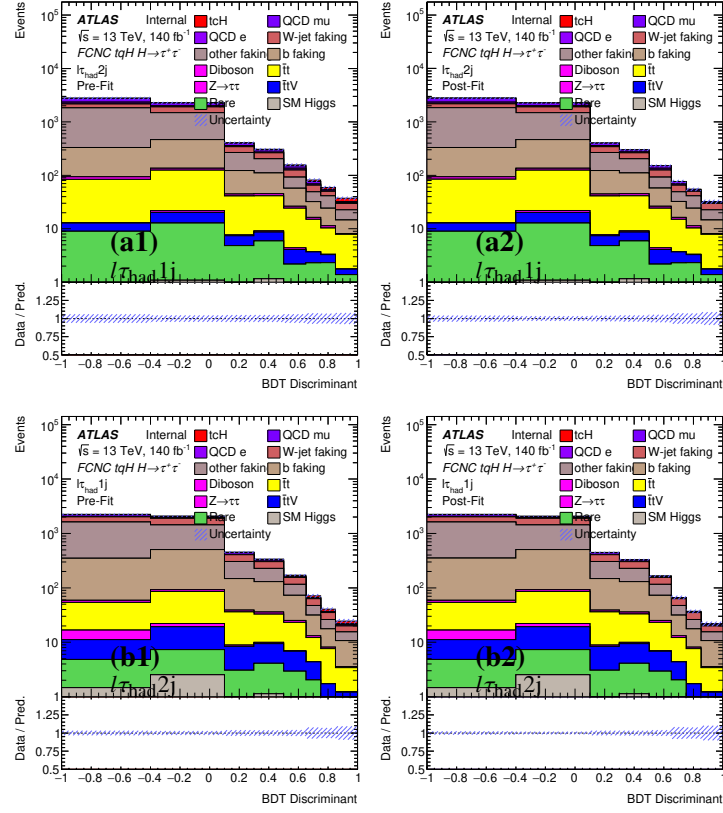


Figure 18: The asimov prefit (left) and postfit (right) BDT distributions in the  $l\tau_{\text{had}}1j$  (a1-2) and  $l\tau_{\text{had}}2j$  (b1-2)

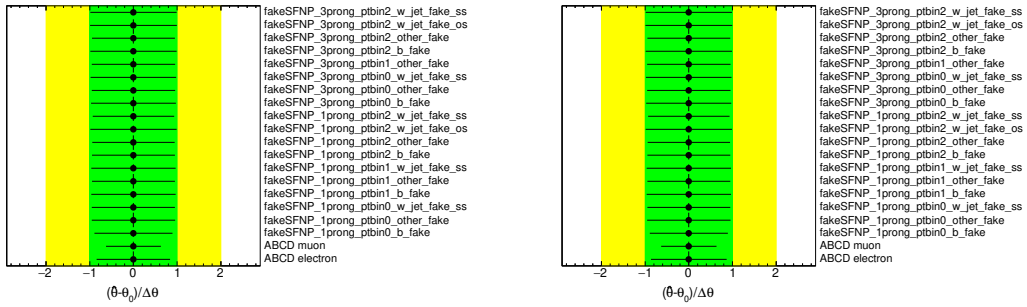


Figure 19: The asimov fit pull distributions of different NPs for  $\tau_{\text{had}}\tau_{\text{had}}$  channels (left) combined and lepton channels combined (right).

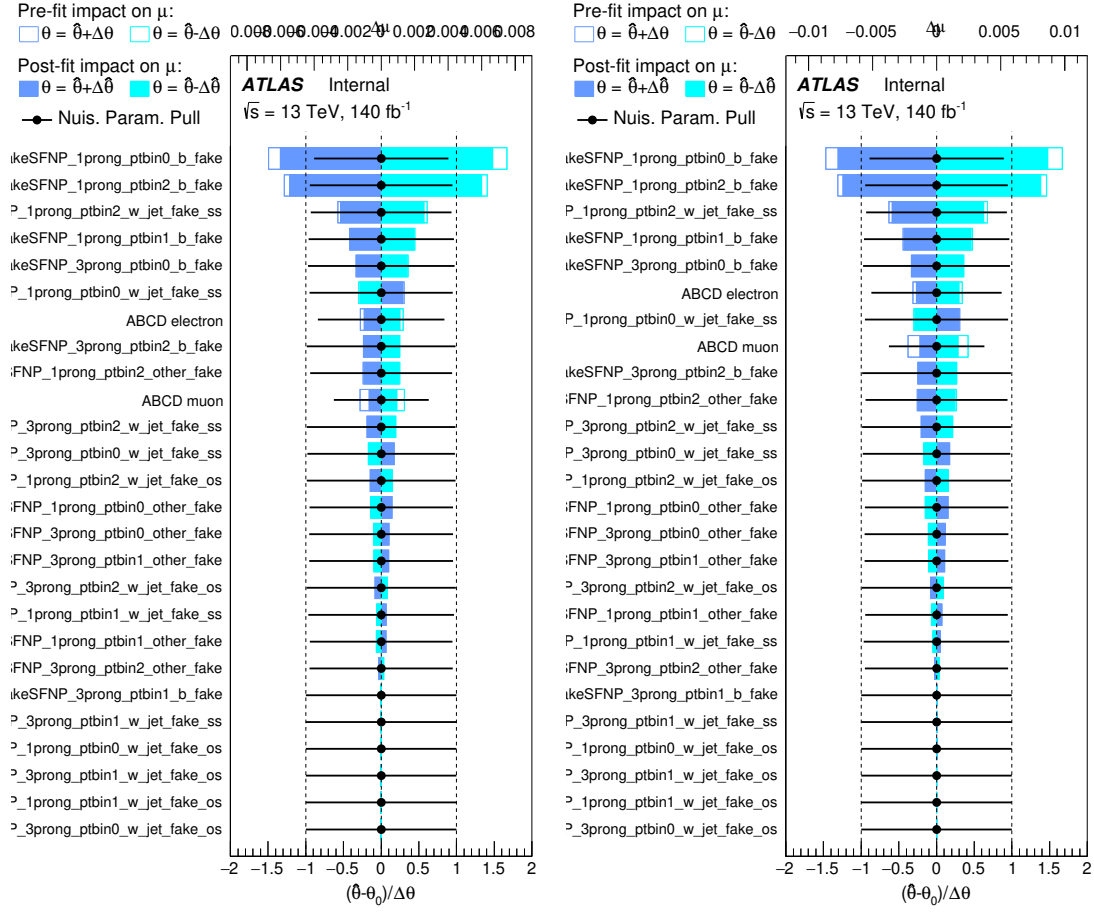


Figure 20: The asimov fit ranking of the top 25 NPs for lepton channels in terms of tuH (left) and tcH (right). The scale of the relative impact on  $\mu$  (the pull) of the NPs is shown on the top (bottom) axis.

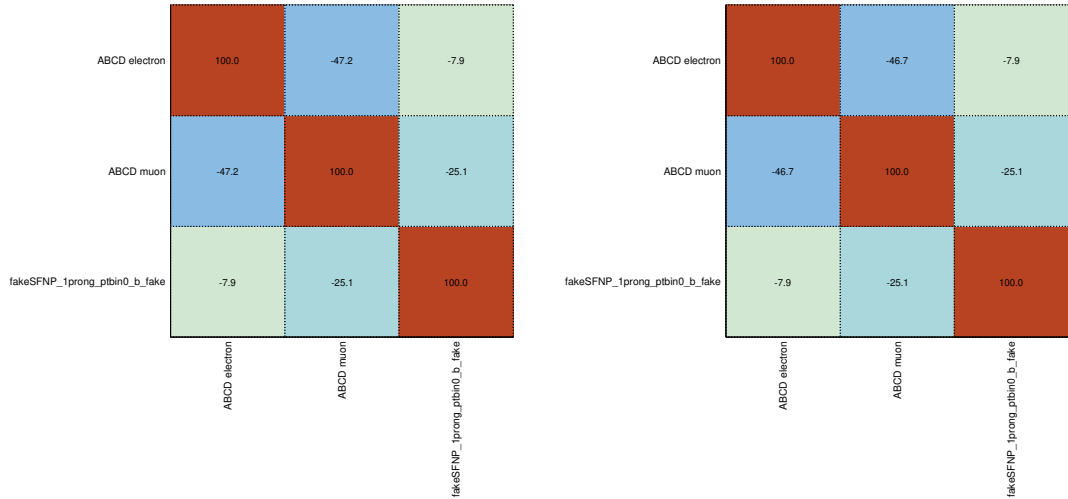


Figure 21: The asimov fit correlation matrix (%) of different NPs, with a threshold of 20% for  $\tau_{\text{had}}\tau_{\text{had}}$  channels (left) combined and lepton channels combined (right).

## 12 Results

The significance of any small observed excess in data is evaluated by quoting the  $p$ -values to quantify the level of consistency of the data with the BR=0 hypothesis. The asymptotic approximation in [76] is used. The test statistic used for the exclusion limits derivation is the  $\tilde{q}_\mu$  test statistic and for the  $p$ -values the  $q_0$  test statistic<sup>4</sup> [76].

The 95% CL upper limits on tqH interaction with BR( $t \rightarrow Hq$ ) = 0.2% as reference are given in Tab. ??.

The best asimov fit values with S+B hypothesis are given in Tab. ??

Table 16: The expected 95% CL exclusion upper limits on BR( $t \rightarrow Hc$ ) and BR( $t \rightarrow Hu$ ) (0.2%) with the Asimov (B-only).

	$l\tau_{\text{had}}2j$	$l\tau_{\text{had}}1j$	STH $\tau_{\text{lep}}\tau_{\text{had}}$
$\bar{t}t \rightarrow bWcH$	$1.94^{+0.77}_{-0.54}$	$1.85^{+0.74}_{-0.52}$	$3.16^{+1.24}_{-0.88}$
$cg \rightarrow tH$	/	/	/
tcH merged signal	$1.89^{+0.75}_{-0.53}$	$1.78^{+0.71}_{-0.50}$	$2.90^{+1.14}_{-0.81}$
$\bar{t}t \rightarrow bWuH$	$1.78^{+0.71}_{-0.50}$	$1.74^{+0.69}_{-0.49}$	$3.03^{+1.19}_{-0.85}$
$ug \rightarrow tH$	$11.17^{+4.48}_{-3.12}$	$8.51^{+3.41}_{-2.38}$	$5.48^{+2.19}_{-1.53}$
tuH merged signal	$1.54^{+0.61}_{-0.43}$	$1.45^{+0.58}_{-0.40}$	$2.00^{+0.79}_{-0.56}$
	TTH $\tau_{\text{lep}}\tau_{\text{had}}$	$l\tau_{\text{had}}\tau_{\text{had}}$	Combined
$\bar{t}t \rightarrow bWcH$	$1.44^{+0.57}_{-0.40}$	$0.29^{+0.13}_{-0.08}$	$0.27^{+0.12}_{-0.08}$
$cg \rightarrow tH$	/	$3.66^{+1.60}_{-1.02}$	$3.60^{+1.57}_{-1.00}$
tcH merged signal	$1.38^{+0.55}_{-0.39}$	$0.27^{+0.12}_{-0.07}$	$0.26^{+0.11}_{-0.07}$
$\bar{t}t \rightarrow bWuH$	$1.35^{+0.53}_{-0.38}$	$0.27^{+0.12}_{-0.07}$	$0.25^{+0.11}_{-0.07}$
$ug \rightarrow tH$	$5.56^{+2.20}_{-1.55}$	$0.79^{+0.34}_{-0.22}$	$0.76^{+0.33}_{-0.21}$
tuH merged signal	$1.09^{+0.43}_{-0.30}$	$0.20^{+0.09}_{-0.06}$	$0.19^{+0.08}_{-0.05}$

The search for the FCNC decay  $t \rightarrow Hq$ ,  $H \rightarrow \tau\tau$  with the ATLAS detector at the LHC using 13 TeV data was presented in this note. The best-fit values for BR( $t \rightarrow Hc$ ) and BR( $t \rightarrow Hu$ ) are found to be

<sup>4</sup> The definition of the test statistics used in this search is the following:

$$\tilde{q}_\mu = \begin{cases} -2 \ln(\mathcal{L}(\mu, \hat{\theta}) / \mathcal{L}(0, \hat{\theta})) & \text{if } \hat{\mu} < 0 \\ -2 \ln(\mathcal{L}(\mu, \hat{\theta}) / \mathcal{L}(\hat{\mu}, \hat{\theta})) & \text{if } 0 \leq \hat{\mu} \leq \mu \\ 0 & \text{if } \hat{\mu} > \mu \end{cases}$$

and

$$q_0 = \begin{cases} -2 \ln(\mathcal{L}(0, \hat{\theta}) / \mathcal{L}(\hat{\mu}, \hat{\theta})) & \text{if } \hat{\mu} \geq 0 \\ 0 & \text{if } \hat{\mu} < 0 \end{cases}$$

where  $\mathcal{L}(\mu, \theta)$  denotes the binned likelihood function,  $\mu$  is the parameter of interest (i.e. the signal strength parameter), and  $\theta$  denotes the nuisance parameters. The pair  $(\hat{\mu}, \hat{\theta})$  corresponds to the global maximum of the likelihood, whereas  $(x, \hat{\theta})$  corresponds to a conditional maximum in which  $\mu$  is fixed to a given value  $x$ .

Table 17: The best asimov fit values with S+B hypothesis.

	$tcH$	$tuH$
$\tau_{\text{had}}\tau_{\text{had}}$	$1.00^{+0.23+0.51}_{-0.22-0.38}$	$1.00^{+0.18+0.44}_{-0.18-0.33}$
leptonic channels	$1.00^{+0.56+X.XX}_{-0.54-X.XX}$	$1.00^{+0.47+X.XX}_{-0.46-X.XX}$

693  $-X.XX^{+X.XX}_{-X.XX}\%$  and  $-X.XX^{+X.XX}_{-X.XX}\%$  respectively, based on  $140\text{ fb}^{-1}$  of data collected from 2015 to 2018.  
 694 The observed (expected) 95% CL upper limits on  $\text{BR}(t \rightarrow Hc)$  and  $\text{BR}(t \rightarrow Hu)$  are found to be  $X.XX\%$   
 695  $(X.XX^{+X.XX}_{-X.XX}\%)$  and  $X.XX\%$  ( $X.XX^{+X.XX}_{-X.XX}\%$ ), respectively.

696 **Appendix**



## References

- [1] ATLAS Collaboration, *Combined Measurement of the Higgs Boson Mass in pp Collisions at  $\sqrt{s}=7$  and 8 TeV with the ATLAS and CMS Experiments*, Phys. Rev. Lett. **114** (2015) 191803, arXiv: [1503.07589 \[hep-ex\]](#).
- [2] S. Glashow, J. Iliopoulos and L. Maiani, *Weak Interactions with Lepton-Hadron Symmetry*, Phys. Rev. D **2** (1970) 1285.
- [3] J. Aguilar-Saavedra, *Top flavor-changing neutral interactions: Theoretical expectations and experimental detection*, Acta Phys. Polon. B **35** (2004) 2695, arXiv: [0409342 \[hep-ph\]](#).
- [4] F. del Aguila, J. A. Aguilar-Saavedra, and R. Miquel, *Constraints on top couplings in models with exotic quarks*, Phys. Rev. Lett. **82** (1999) 1628, arXiv: [9808400 \[hep-ph\]](#).
- [5] J. Aguilar-Saavedra, *Effects of mixing with quark singlets*, Phys. Rev. D **67** (2003) 035003, arXiv: [0210112 \[hep-ph\]](#).
- [6] S. Bejar, J. Guasch and J. Sola, *Loop induced flavor changing neutral decays of the top quark in a general two Higgs doublet model*, Nucl. Phys. B **600** (2001) 21, arXiv: [0011091 \[hep-ph\]](#).
- [7] I. Baum, G. Eilam and S. Bar-Shalom, *Scalar flavor changing neutral currents and rare top quark decays in a two Higgs doublet model 'for the top quark'*, Phys. Rev. D **77** (2008) 113008, arXiv: [0802.2622 \[hep-ph\]](#).
- [8] J. J. Cao et al., *SUSY-induced FCNC top-quark processes at the large hadron collider*, Phys. Rev. D **75** (2007) 075021, arXiv: [0702264 \[hep-ph\]](#).
- [9] G. Eilam et al., *Top quark rare decay  $t \rightarrow ch$  in R-parity violating SUSY*, Phys. Lett. B **510** (2001) 227, arXiv: [0102037 \[hep-ph\]](#).
- [10] G. Lu et al., *The rare top quark decays  $t \rightarrow cV$  in the topcolor-assisted technicolor model*, Phys. Rev. D **68** (2003) 015002, arXiv: [0303122 \[hep-ph\]](#).
- [11] K. Agashe, G. Perez and A. Soni, *Collider signals of top quark flavor violation from a warped extra dimension*, Phys. Rev. D **75** (2007) 015002, arXiv: [0606293 \[hep-ph\]](#).
- [12] B. Yang, N. Liu and J. Han, *Top quark flavor-changing neutral-current decay to a 125 GeV Higgs boson in the littlest Higgs model with T parity*, Phys. Rev. D **89** (2014) 034020, arXiv: [1308.4852 \[hep-ph\]](#).
- [13] K. Agashe and R. Contino, *Composite Higgs-mediated flavor-changing neutral current*, Phys. Rev. D **80** (2009) 075016, arXiv: [0906.1542 \[hep-ph\]](#).

- [14] T. P. Cheng and Marc Sher, *Mass Matrix Ansatz and Flavor Nonconservation in Models with Multiple Higgs Doublets*, Phys. Rev. D **35** (1987) 3484.
- [15] Wei-Shu Hou, *Tree level  $t \rightarrow ch$  or  $h \rightarrow t\bar{c}$  decays*, Phys. Lett. B **296** (1992) 179.
- [16] Federico Demartin, Fabio Maltoni, Kentarou Mawatari, Marco Zaro, *Higgs production in association with a single top quark at the LHC*, (2015), arXiv: [1504.00611 \[hep-ph\]](#).
- [17] ATLAS Collaboration, *Search for top quark decays  $t \rightarrow qH$ , with  $H \rightarrow \gamma\gamma$ , in  $\sqrt{s} = 13$  TeV  $pp$  collisions using the ATLAS detector*, JHEP (2017) 129, arXiv: [1707.01404 \[hep-ex\]](#).
- [18] ATLAS Collaboration, *Search for flavor-changing neutral currents in top quark decays  $t \rightarrow Hc$  and  $t \rightarrow Hu$  in multilepton final states in proton–proton collisions at  $\sqrt{s} = 13$  TeV with the ATLAS detector*, Phys. Rev. D (2018) 36, arXiv: [1805.03483 \[hep-ex\]](#).
- [19] ATLAS Collaboration, *Search for top-quark decays  $t \rightarrow qH$  with 36 fb<sup>-1</sup> of  $pp$  collision data at  $\sqrt{s}=13$  TeV with the ATLAS detector*, (), arXiv: [1812.11568 \[hep-ex\]](#).
- [20] CMS Collaboration, *Search for the flavor-changing neutral current interactions of the top quark and the Higgs boson which decays into a pair of  $b$  quarks at  $\sqrt{s} = 13$  TeV*, JHEP **06** (2018) 102, arXiv: [1712.02399 \[hep-ex\]](#).
- [21] Celine Degrande, Fabio Maltoni, Jian Wang, Cen Zhang, *Automatic computations at next-to-leading order in QCD for top-quark flavor-changing neutral processes*, Phys. Rev. D (2015) 6, arXiv: [1412.5594 \[hep-ex\]](#).
- [22] ATLAS Collaboration, *The ATLAS Experiment at the CERN Large Hadron Collider*, JINST **3** (2008) S08003.
- [23] ATLAS Collaboration, *ATLAS Insertable B-Layer Technical Design Report*, CERN-LHCC-2010-013; ATLAS-TDR-19, 2010, URL: <https://cds.cern.ch/record/1291633>.
- [24] ATLAS Collaboration, *Luminosity determination in  $pp$  collisions at  $\sqrt{s} = 8$  TeV using the ATLAS detector at the LHC*, (2016), arXiv: [1608.03953 \[hep-ex\]](#).
- [25] Celine Degrande et al., *Automatic computations at next-to-leading order in QCD for top-quark flavor-changing neutral processes*, Phys. Rev. D **91** (2015) 034024, arXiv: [1412.5594 \[hep-ph\]](#).
- [26] Celine Degrande et al., *Effective theory for top flavor changing interactions*, 2016, URL: <https://feynrules.irmp.ucl.ac.be/wiki/TopFCNC>.
- [27] J. Alwall et al., *The automated computation of tree-level and next-to-leading order differential cross sections, and their matching to parton shower simulations*, JHEP **07** (2014) 079, arXiv: [1405.0301 \[hep-ph\]](#).

- [28] T. Sjostrand et al., *An introduction to PYTHIA 8.2*, Comp. Phys. Commun. **191** (2015) 159, arXiv: [1410.3012 \[hep-ph\]](#).
- [29] ATLAS Collaboration, *ATLAS Pythia 8 tunes to 7 TeV data*, ATL-PHYS-PUB-2014-021, 2014, URL: <https://cdsweb.cern.ch/record/196641>.
- [30] R. D. Ball et al., *Parton distributions for the LHC Run II*, JHEP **04** (2015) 040, arXiv: [1410.8849 \[hep-ph\]](#).
- [31] C. Oleari, *The POWHEG-BOX*, Nucl. Phys. Proc. Suppl. **205-206** (2010) 36–41, arXiv: [1007.3893 \[hep-ph\]](#).
- [32] T. Gleisberg et al., *Event generation with Sherpa 1.1*, JHEP **02** (2009) 007, arXiv: [0811.4622 \[hep-ph\]](#).
- [33] N. Davidson et al., *Universal interface of TAUOLA: Technical and physics documentation*, Comp. Phys. Commun. **183** (2012) 821.
- [34] S. Agostinelli et al., *GEANT4 - A simulation toolkit*, Nucl. Instrum. Meth. A **506** (2003) 250.
- [35] J. Bellm et al., *Herwig 7.0/Herwig++ 3.0 release note*, Eur. Phys. J. C **76** (2016) 196.
- [36] ATLAS Collaboration, *The simulation principle and performance of the ATLAS fast calorimeter simulation FastCaloSim*, ATL-PHYS-PUB-2010-013, 2010, URL: <http://cds.cern.ch/record/1300517>.
- [37] J Butterworth et al., *Single Boson and Diboson Production Cross Sections in pp Collisions at  $\sqrt{s}=7$  TeV*, ATL-COM-PHYS-2010-695, 2010, URL: <http://cds.cern.ch/record/1287902>.
- [38] M. Czakon and A. Mitov, *Top++: a program for the calculation of the top-pair cross-section at hadron colliders*, Comput. Phys. Commun **185** (2014) 2930, arXiv: [1112.5675 \[hep-ph\]](#).
- [39] D. de Florian et al., *Handbook of LHC Higgs Cross Sections: 4. Deciphering the Nature of the Higgs Sector*, CERN-2017-002-M (2017), arXiv: [1610.07922 \[hep-ph\]](#), URL: <https://cds.cern.ch/record/2227475>.
- [40] J. Alwall et al., *The automated computation of tree-level and next-to-leading order differential cross sections, and their matching to parton shower simulations*, JHEP **07** (2014) 079, arXiv: [1405.0301 \[hep-ph\]](#).
- [41] M. Aliev et al., *HATHOR - HAdronic Top and Heavy quarks crOss section calculatoR*, Comput. Phys. Commun **182** (2011) 1034, arXiv: [1007.1327 \[hep-ph\]](#).
- [42] P. Kant et al., *HATHOR for single top-quark production: Updated predictions and uncertainty estimates for single top-quark production in hadronic collisions*, Comput. Phys. Commun **191** (2015) 74, arXiv: [1406.4403 \[hep-ph\]](#).

- [43] N. Kidonakis,  
*Two-loop soft anomalous dimensions for single top quark associated production with a  $W^-$  or  $H^-$ ,*  
 Phys. Rev. D **82** (2010) 054018, arXiv: [1005.4451 \[hep-ph\]](#).
- [44] J. Pumplin et al.,  
*New Generation of Parton Distributions with Uncertainties from Global QCD Analysis,*  
 JHEP **07** (2002) 012, arXiv: [0201195 \[hep-ph\]](#).
- [45] M. Cacciari, G. P. Salam, and G. Soyez, *The Anti- $k(t)$  jet clustering algorithm,*  
 JHEP **04** (2008) 063, arXiv: [0802.1189 \[hep-ph\]](#).
- [46] ATLAS Collaboration, *Tagging and suppression of pileup jets with the ATLAS detector,*  
 ATLAS-CONF-2014-018, 2014, URL: <http://cds.cern.ch/record/1700870>.
- [47] ATLAS Collaboration, *Optimisation of the ATLAS  $b$ -tagging performance for the 2016 LHC Run,*  
 ATL-PHYS-PUB-2016-012, 2016, URL: <https://cds.cern.ch/record/2160731>.
- [48] *Electron and Photon Selection and Identification for Run2,* Accessible on 2017-11-24,  
 URL: <https://twiki.cern.ch/twiki/bin/view/AtlasProtected/EGammaIdentificationRun2>.
- [49] *Official Isolation Working Points,* Accessible on 2017-11-24, URL: <https://twiki.cern.ch/twiki/bin/viewauth/AtlasProtected/IsolationSelectionTool#Leptons>.
- [50] *MuonSelectionTool,* Accessible on 2017-11-24,  
 URL: <https://twiki.cern.ch/twiki/bin/view/Atlas/MuonSelectionTool>.
- [51] ATLAS Collaboration, *Reconstruction, Energy Calibration, and Identification of Hadronically  
 Decaying Tau Leptons in the ATLAS Experiment for Run-2 of the LHC,*  
 ATL-PHYS-PUB-2015-045, 2015, URL: <https://cds.cern.ch/record/2064383>.
- [52] ATLAS Collaboration,  
*Jet energy measurement with the ATLAS detector in proton-proton collisions at  $\sqrt{s} = 7$  TeV,*  
 Eur. Phys. J. C **73** (2013) 2304, arXiv: [1112.6426 \[hep-ex\]](#).
- [53] *TauAnalysisTools,* Accessible on 2017-11-24,  
 URL: <https://svnweb.cern.ch/trac/atlasoff/browser/PhysicsAnalysis/TauID/TauAnalysisTools/tags/TauAnalysisTools-00-02-62/README.rst>.
- [54] *2017 Tau Recommendations,* Accessible on 2017-11-24, URL: <https://twiki.cern.ch/twiki/bin/view/AtlasProtected/TauRecommendationsMoriond2017>.
- [55] *Usage of Missing  $ET$  in analyses: rebuilding and systematics,* Accessible on 2017-11-24,  
 URL: <https://twiki.cern.ch/twiki/bin/viewauth/AtlasProtected/METUtilities>.
- [56] James, F. and Roos, M., *Minuit: A System for Function Minimization and Analysis of the  
 Parameter Errors and Correlations,* Comput. Phys. Commun. **10** (1975) 343,  
 URL: <http://lcgapp.cern.ch/project/cls/work-packages/mathlibs/minuit>.

- [57] ATLAS Collaboration, *Measurement of the  $H \rightarrow \tau^+\tau^-$  cross-section in 13TeV Collisions with the ATLAS Detector*, ATL-COM-PHYS-2017-446, 2017, URL: <https://cds.cern.ch/record/2261605>.
- [58] ATLAS Collaboration, *Search for the Associated Production of a Higgs Boson and a Top Quark Pair in multilepton final states in  $80\text{ fb}^{-1}$   $pp$  Collisions at  $\sqrt{s} = 13\text{ TeV}$  with the ATLAS Detector*, ATL-COM-PHYS-2018-410, 2018, URL: <https://cds.cern.ch/record/2314122>.
- [59] J. Friedman, *Stochastic gradient boosting*, Comput. Stat. Data Anal. **38** (2002) 367.
- [60] A. Hoecker et al., *TMVA - Toolkit for Multivariate Data Analysis*, PoS A CAT **040** (2007), arXiv: [0703039](https://arxiv.org/abs/0703039) [physics].
- [61] *TRExFitter*, Accessible on 2017-11-24, URL: <https://gitlab.cern.ch/TRExStats/TRExFitter>.
- [62] ATLAS Collaboration, *Electron efficiency measurements with the ATLAS detector using the 2015 LHC proton–proton collision data*, ATLAS-CONF-2016-024, 2016, URL: <https://cds.cern.ch/record/2157687>.
- [63] ATLAS Collaboration, *Jet Calibration and Systematic Uncertainties for Jets Reconstructed in the ATLAS Detector at  $\sqrt{s} = 13\text{ TeV}$* , ATL-PHYS-PUB-2015-015, 2015, URL: <https://cds.cern.ch/record/2037613>.
- [64] ATLAS Collaboration, *Performance of missing transverse momentum reconstruction for the ATLAS detector in the first proton-proton collisions at  $\sqrt{s} = 13\text{ TeV}$* , ATL-PHYS-PUB-2015-027, 2015, URL: <https://cds.cern.ch/record/2037904>.
- [65] ATLAS Collaboration, *Expected performance of the ATLAS  $b$ -tagging algorithms in Run-2*, ATL-PHYS-PUB-2015-022, 2015, URL: <https://cds.cern.ch/record/2037697>.
- [66] ATLAS Collaboration, *Calibration of the performance of  $b$ -tagging for  $c$  and light-flavour jets in the 2012 ATLAS data*, ATLAS-CONF-2014-046, 2014, URL: <https://cds.cern.ch/record/1741020>.
- [67] ATLAS Collaboration, *Calibration of  $b$ -tagging using dileptonic top pair events in a combinatorial likelihood approach with the ATLAS experiment*, ATLAS-CONF-2014-004, 2014, URL: <https://cds.cern.ch/record/1664335>.
- [68] ATLAS Collaboration, *Studies on top-quark Monte Carlo modelling with Sherpa and MG5\_aMC@NLO*, ATL-PHYS-PUB-2017-007, 2017, URL: <https://cds.cern.ch/record/2261938>.
- [69] ATLAS Collaboration, *Search for flavor-changing neutral current  $t \rightarrow Hq$  ( $q=u,c$ ) decays, with  $H \rightarrow b\bar{b}$ , in the lepton+jets final state in  $pp$  collisions at  $\sqrt{s} = 13\text{ TeV}$  with the ATLAS detector*, ATL-COM-PHYS-2017-346, 2017, URL: <https://cds.cern.ch/record/2257631>.
- [70] J. M. Campbell and R. K. Ellis, *An Update on vector boson pair production at hadron colliders*, Phys. Rev. D **60** (1999) 113006, arXiv: [9905386](https://arxiv.org/abs/9905386) [hep-ph].

- 872 [71] N. Kidonakis, *Next-to-next-to-leading-order collinear and soft gluon corrections for t-channel*  
873 *single top quark production*, Phys. Rev. D **83** (2011) 091503, arXiv: [1103.2792 \[hep-ph\]](#).
- 874 [72] N. Kidonakis, *NNLL resummation for s-channel single top quark production*,  
875 Phys. Rev. D **81** (2010) 054028, arXiv: [1001.5034 \[hep-ph\]](#).
- 876 [73] M. V. Garzelli et al.,  *$t\bar{t}W^\pm$  and  $t\bar{t}Z$  Hadroproduction at NLO accuracy in QCD with Parton*  
877 *Shower and Hadronization effects*, JHEP **1211** (2012) 056, arXiv: [1208.2665 \[hep-ph\]](#).
- 878 [74] J. M. Campbell and R. K. Ellis,  *$t\bar{t}W^\pm$  production and decay at NLO*, JHEP **1207** (2012) 052,  
879 arXiv: [1204.5678 \[hep-ph\]](#).
- 880 [75] LHC Higgs Cross Section Working Group,  
881 *Handbook of LHC Higgs Cross Sections: 1. Inclusive Observables*, (2011),  
882 arXiv: [1101.0593 \[hep-ph\]](#).
- 883 [76] G. Cowan, K. Cranmer, E. Gross and O. Vitells,  
884 *Asymptotic formulae for likelihood-based tests of new physics*, Eur. Phys. J. C **71** (2011) 1554,  
885 arXiv: [1007.1727 \[physics.data-an\]](#).

## List of contributions

- Boyang Li: main analyser, signal generation; ntuple production; fake tau estimation; BDT analysis; systematics; fit; support note.
- Weiming Yao: main analyser, `ttHML` ntuple skimming and support; fake tau estimation; BDT analysis; cross check; support note.
- MingMing Xia: main analyser, `xTauFramework` n-tuple production; production validation.
- Xin Chen: Supervisor of Boyang Li and MingMing Xia